Regional CO$_2$ inversions with LUMIA, the Lund University Modular Inversion Algorithm, v1.0

Guillaume Monteil[1] and Marko Scholze[1]

[1]Department of Physical Geography and Ecosystem Science, Lund University, Lund, Sweden

Correspondence: Guillaume Monteil (guillaume.monteil@nateko.lu.se)

Abstract. Atmospheric inversions are commonly used for estimating large-scale (continental to regional) net sources and sinks of CO$_2$ and other stable atmospheric tracers from their observed concentrations. Recently, there has been an increasing demand from stakeholders for robust estimates of greenhouse gases at country-scale (or higher) resolution, in particular in the framework of the Paris agreement. This increase in resolution is in theory enabled by the growing availability of observations

5 from surface in-situ networks (such as ICOS in Europe) and from remote sensing products (OCO-2, GOSAT-2). The increase in the resolution of inversions is also a necessary step to provide efficient feedback to the process-based (bottom-up) modelling community (vegetation models, fossil fuel emission inventories). This, however, calls for new developments in the inverse modelling systems, mainly in terms of diversification of the inversion approaches, shift from global to regional inversions, and improvement in the computational efficiency,

10 We have developed the Lund University Modular Inversion Algorithm (LUMIA) as a tool to address some of these new developments. LUMIA is meant to be a platform for inverse modelling developments at Lund University. It aims at being a flexible, yet simple and easy to maintain set of tools that modellers can combine to build inverse modelling experiments. It is in particular designed to be transport model agnostic, which should facilitate isolating the transport model errors from those introduced by the inversion setup itself. Here, we briefly describe the motivations for developing LUMIA as well as the under-

15 lying development principles, current status and future prospects. We present a first LUMIA inversion setup for a regional CO$_2$ inversions over Europe, based on a new coupling between the Lagrangian FLEXPART (high resolution foreground transport) and the global coarse resolution TM5 transport models, using in-situ data from surface and tall tower observation sites.

1 Introduction

The accumulation of greenhouse gases in the atmosphere is the main driver of climate change. The largest contribution of

20 anthropogenic activities to global warming is through the release of fossil carbon (mainly as CO$_2$) to the atmosphere, but other human activities such as land use change (for agriculture, deforestation, etc.) also play a significant role. The climate forcings from this increased CO$_2$ concentration is likely to induce feedbacks through reactions of the terrestrial ecosystems and of the oceans (Stocker et al., 2013). Our capacity to correctly predict climate change, anticipate and mitigate its effects depends therefore largely on our capacity to model and predict the evolution of carbon exchanges between the atmosphere and other

25 reservoirs.

For future climate simulations, the only available option is through "direct" (bottom-up) modelling of the different components of the biogeochemical cycles, i.e. using models (numerical or statistical) that simulate, as accurately as possible (given the precision requirements of the simulation), greenhouse gas fluxes to and from the atmosphere. For past periods, however, the "inverse" (top-down) approach is also possible, in which the greenhouse gas fluxes are diagnosed from their observed impact on atmospheric greenhouse gas concentrations.

Direct and inverse approaches are complementary, the former can provide detailed estimates of the spatial and temporal variability of the fluxes, but often with large uncertainties on the total fluxes Sitch et al. (2015) . On the contrary, inverse approaches provide robust estimates of total fluxes at large scales consistent with the observations (e.g. Gurney et al. (2002)), but with poor sensitivity to smaller scales (e.g. Peylin et al. (2013)).

An atmospheric inverse model typically couples an atmospheric transport model (which computes the relationships between fluxes and concentrations) with an inversion algorithm, whose task is to determine the most likely set of fluxes, within some prior constraints and given the information from an observation ensemble (in a Bayesian approach). In practice, inversions are complex codes, computationally heavy. The complexity arises in a large part from the necessity to combine large quantities of informations from sometimes very heterogeneous datasets (various types of observations, flux estimates, meteorological forcings, etc.). The computational weight depends largely on that of the underlying transport model, which usually needs to be ran a large number of times (iteratively or as an ensemble).

In recent years, the availability of observations has grown by orders of magnitude, with the deployment of high-density surface observation networks (such as the Integrated Carbon Observation System, ICOS, in Europe) and the fast developments in satellite retrievals of tropospheric greenhouse gas concentrations (GOSAT, OCO-2, etc.). Meanwhile, the demand for inversions is increasing, in particular from stakeholders such as regional, national or trans-national governments who are interested in country-scale inversions as a means of quantifying their carbon emissions, in connection with emission reduction targets as defined in the Paris agreement (Ciais et al., 2015).

This context puts strains on the existing inverse models. The larger availability of high quality data means that fluxes can be constrained at finer scales, but it also means that models of higher definition and precision must be used. The development of regional inversions (of varying scales) allows in theory an efficient usage of high resolution data while preserving a reasonable computational cost, but comes with specific challenges such as the need of more boundary conditions and the lack of options for cross-validation when the resolution increases and the domain size shrinks. The demands from various stakeholders (policy makers, bottom-up modellers, medias, etc.) also call for developments in the inversion techniques, with for instance a more pronounced focus on the quantification of anthropogenic sources (Ciais et al., 2015) or the optimization of ecosystem models parameters instead of CO_2 fluxes in carbon cycle data assimilation systems (CCDAS) (Kaminski et al., 2013).

To enable such progress in the method and quality of the inversions, it is important to have a robust and flexible tool. The purpose of LUMIA (Lund University Modular Inversion Algorithm) is to be not an integrated, well defined inverse model, but a development platform for top-down experiments. LUMIA was developed from the start as a model-agnostic inversion tool, with a clear isolation of the data stream between the transport model and the optimization algorithm in an interface module. One of the main aims is to eventually allow a better characterization of the uncertainty associated to the transport model. Strong

emphasis was put on the usability (low barrier entry code for newcomers, high degree of modularity to allow users to build their experiments in a very flexible way) and sustainability of the code (small, easily replaceable one-tasked modules instead of large multi-option ones).

This paper presents the general concepts of LUMIA, as well as a first application of regional (European) CO_2 inver-
sions for Europe. The inversions use in-situ CO_2 observations from European tall towers (now part of the ICOS network, see https://www.icos-ri.eu) and rely on a regional transport model based on a new coupling between the FLEXPART Lagrangian particle dispersion model (Seibert and Frank, 2004; Pisso et al., 2019) (foreground, high resolution transport) and TM5-4DVAR (Meirink et al., 2008; Basu et al., 2013b) (background concentrations). The paper is organized as follows: First, Section 2presents the LUMIA framework (general principles and architecture). Then Section 3 presents the specific inverse
modelling setup used here (including the FLEXPART-TM5 coupling). Sections 4 and 5 present the results from two set of inversions (against synthetic and real observations). Finally, a short discussion summarises the main outcomes of the paper in Section 6.

2 The LUMIA framework

2.1 General inversion principles, and implications on the code structure

The general principle of an atmospheric inversion is to determine the most likely estimate of a set of variables controlling the atmospheric content and distribution of a tracer (typically sources and sinks, but also initial or boundary conditions), given a set of observations of that tracer's distribution in the atmosphere. The link between the set of parameters to optimize (control vector $\mathbf{x}$, of dimension $n_\mathbf{x}$) and the observed concentrations (observation vector $\mathbf{y}$, of dimension $n_\mathbf{y}$) is established by a numerical model of the atmospheric transport (and of any other physical process relating the state and observation vectors):

$$\mathbf{y} + \varepsilon_y = H(\mathbf{x} + \varepsilon_x) + \varepsilon_H \tag{1}$$

H is the observation operator, which includes the atmospheric transport model itself but also any additional step between the physical quantities represented by $\mathbf{x}$ and $\mathbf{y}$. The error terms ε_y, ε_x and ε_H are respectively the observation error, the control vector error and the model representation error (see Section 3.1).

In the simplest cases, the system can be solved for $\mathbf{x}$ analytically, but most often inversions use the Bayesian inference approach: the optimal control vector $\hat{\mathbf{x}}$ is the one that allows the best statistical compromise between fitting the observations and limiting the departure from a prior estimation of the control vector $\mathbf{x_b}$ (accounting for the (prescribed) uncertainties in the

observations and the prior). Mathematically, this means finding the vector $\hat{\mathbf{x}}$ that minimizes a cost function $J(\mathbf{x})$ defined (in our case) as

$$
\begin{aligned}
J(\mathbf{x}) &= \frac{1}{2}\left(\mathbf{x} - \mathbf{x_b}\right)^T \mathbf{B}^{-1}\left(\mathbf{x} - \mathbf{x_b}\right) \\
&+ \frac{1}{2}\sum_j \left(\mathbf{Hx} - \mathbf{y_j}\right)^T \mathbf{R}^{-1}\left(\mathbf{Hx} - \mathbf{y_j}\right) \\
&= J_{\mathbf{b}} + J_{obs}
\end{aligned}
\tag{2}
$$

where the prior ($\mathbf{B}$) and observation ($\mathbf{R}$) error covariance matrices weigh the relative contributions to the cost function of each departure from each prior control variable x_b^i and from each observation y^j. The optimal control vector $\hat{\mathbf{x}}$ is solved for analytically (for small scale problems) or approximated step-wise (variational and ensemble approaches are most common (Rayner et al., 2018)).

An inversion system is therefore the combination of an observation operator (i.e. transport model, sampling operator, etc.), an inversion technique and a set of assumptions on the prior values of the variables to estimates, their uncertainties and the uncertainties of the observations. Each of these components introduces its own share of uncertainty, which makes the results harder to interpret: which feature of the solution is real, and which is introduced by e.g. the transport model, or incorrect assumptions on some uncertainties?

These questions are difficult to address with inversion systems tightly integrating a transport model and an implementation of a specific inversion technique. LUMIA is therefore developed as a flexible inversion library, with a clear isolation between the transport model and the inversion algorithm itself. LUMIA is primarily designed of a collection of modules, as simple and independent as reasonable, that can be used as basic elements to construct (inverse or forward) transport modelling experiments.

While the name "LUMIA" refers to that code library, its development (and first application) stem from the need of performing regional CO_2 inversions based on observations using in-situ data from the ICOS network. At this stage, the existing code is therefore largely limited to that regional inversion setup. The distinction between the LUMIA inversion library and the specific LUMIA setup presented in the rest of this document is therefore somewhat theorerical but we maintain the prospect of future developments.

2.2 Architecture and technical implementation

The flowchart in Figure 1 represents the data flow in our current inversion setup (see Section 3). The blocks within the black box are part of the actual LUMIA library, while blocs outside are either pre-processing steps (import of fluxes and observations) or external tools called by LUMIA (transport model).

Among the LUMIA modules (in green), two are primarily databases. The *optimData* module stores data in the optimization space (control vectors (prior, posterior and intermediate steps), coordinates of the control variables (lat, lon, time, category), uncertainties) ; the *obsdb* module stores data in the observations space: observation vector, observations coordinates and un-

115 certainties, model estimates for the observations, etc. (the exact list of field stored here is totally user-dependent. In our case the path to the observation response functions are stored (See Section 3.2.1), but one could also store for instance some data quality flag, or different model estimates for a same observation dataset). The two modules include save/load functions and can be instantiated independently, which allows their use in pre- and post-processing stages (preparation of the inversion inputs, analysis of the results, diagnostics, etc.).

120 The core of the inversion setup is the *Optimizer* module, which implements the actual steps of the optimization algorithm (as described in Section 3.1). It does not itself perform any calculation but calls routines from the other modules and controls the data flow between them. The *minimizer* module handles the communication with an external conjugate gradient executable.

The *transport* module is the main interface between the inversion algorithm and the actual transport model. It constructs the transport model input based on a given control vector, triggers the actual transport modelling runs and constructs model-data 125 mismatch vectors based on transport model output. The module is also designed so as to be instantiatable independently, for instance to allow forward transport runs.

The two pre-processing modules (in blue on the diagram) contain routines to import fluxes and observations from various data providers (handling of different file formats, units conversions, etc.), and are in charge of filling in the databases in *obsdb* and *optimData*. These preprocessing steps typically represent a large fraction of the total code of (any) inversion setup, but are 130 very user- and application-specific. We chose to explicitly exclude them from the LUMIA library, as the benefit of including them is far outweighed by the associated code maintenance cost. These pre-processing steps are also not necessarily performed at the same time, and on the same computer, as the inversion itself.

The execution of the actual inversion is controlled by a master python script, written by the user and for which an example is provided in SI. The transport operator itself (purple box) is formally independent of the LUMIA library, nonetheless our 135 transport script, which relies on pre-computed observation response functions, is distributed and can be used as an example (in SI).

3   Inversion setup

Our test inversion setup is designed to optimize the monthly net atmosphere-ecosystem carbon flux (NEE, Net Ecosystem Exchange) over Europe at a target horizontal resolution of $0.5°$, using CO_2 observations from the European ICOS network 140 (or similar/precursor sites). Two series of inversions are presented: First, a series of Observing System Synthetic Experiments (OSSEs), using known truth and synthetic observations; then a series of inversions constrained by real observations. All the inversions are performed on a domain ranging from $15°W$, $33°N$ to $35°E$, $73°N$ (illustrated in Figure 2, and hereafter referred to as the Regional Inversion Domain, RID) and cover the year 2011. The following sections describe the inversion technique, the transport model and the problem constraints (prior fluxes and observations).
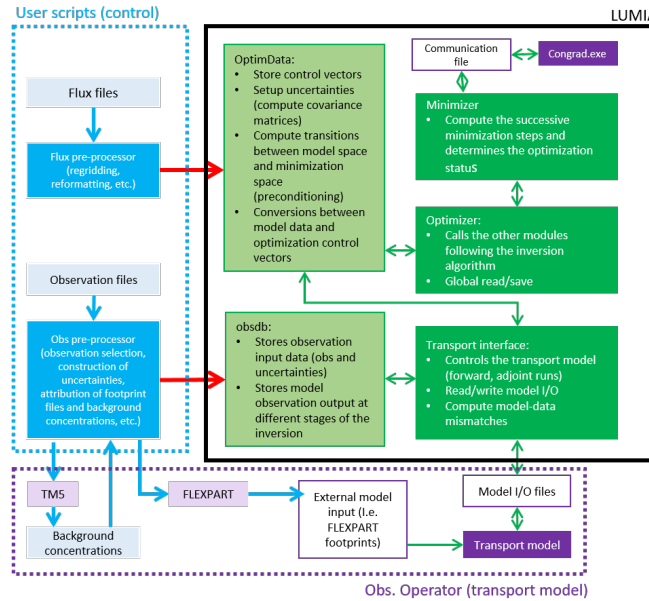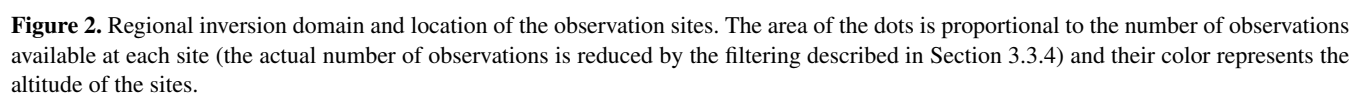
Figure 1. Inversion flow diagram. Green boxes are LUMIA modules, purple boxes are external codes and blue boxes are pre-processing scripts, typically user- and application-specific. The black thick line marks the limits of LUMIA itself. The red arrows show the flow of data in the inversion setup phase and the green arrows show the data flow during the inversion. The inversion inputs are prepared in a preparation phase (blue arrows), which involves external models (FLEXPART and TM5). The transport model used in the inversion is considered an external code (here is is a simple python script that reads in observations, fluxes and footprints, but a full transport model could be plugged in instead).

3.1 Inversion approach

We use a Bayesian variational inversion algorithm, similar to that used in TM5-4DVAR inversions (Basu et al., 2013b; Meirink et al., 2008). In a variational inversion, the minimum of the cost function $J(\mathbf{x})$ (Equation 2) is solved for iteratively:

1. An initial "prior" run is performed to compute the concentrations ($\mathbf{y_m} = \mathbf{Hx_b}$) corresponding to the prior control vector $\mathbf{x_b}$ (since the transport is linear, $H(\mathbf{x}) \equiv \mathbf{Hx}$).

2. The local cost function ($J(\mathbf{x} = \mathbf{x_b})$) and cost function gradient ($\nabla_{\mathbf{x}} J(\mathbf{x} = \mathbf{x_b})$) are computed.

3. A control vector increment ($\delta\mathbf{x}$) is deduced from the gradient, and the process is repeated from step 1 (with $\mathbf{x} = \mathbf{x_b} + \delta\mathbf{x}$), until a convergence criterion is reached.

The control vector increments are computed using an external library implementing the Lanczos algorithm (Lanczos, 1950). For efficiency (reduction of the number of iterations) and practicality (reduction of the number of large matrix multiplications) reasons, the optimization is performed on the preconditioned variable $\omega = \mathbf{B}^{-1/2}(\mathbf{x} - \mathbf{x_b})$ (following Courtier et al. (1994)

6

Figure 2. Regional inversion domain and location of the observation sites. The area of the dots is proportional to the number of observations available at each site (the actual number of observations is reduced by the filtering described in Section 3.3.4) and their color represents the altitude of the sites.

and similar to the implementation in Basu et al. (2013b). Equation 2 then becomes

$$J(\omega) = \frac{1}{2}\omega^T\omega + \frac{1}{2}\left(\mathbf{HB}^{1/2}\omega + \mathbf{d_0}\right)^T\mathbf{R}^{-1}\left(\mathbf{HB}^{1/2}\omega + \mathbf{d_0}\right) \tag{3}$$

with $\mathbf{d_0} = \mathbf{Hx_b} - \mathbf{y}$ the prior model-data mismatches. In this formulation, the cost function gradient is given by

$$\nabla_\omega J = \omega + \mathbf{B^{T/2}H^TR^{-1}}\left(\mathbf{Hx} - \mathbf{y}\right)$$
$$= \omega + \mathbf{B^{T/2}}\nabla_\mathbf{x}J_{obs} \tag{4}$$

160   The non-preconditioned observational cost function gradient $\nabla_x J_{obs} = \mathbf{H^TR^{-1}}\left(\mathbf{Hx} - \mathbf{y}\right)$ is computed using the adjoint technique (Errico, 1997). The transformation matrix $\mathbf{B^{1/2}}$ is obtained by eigen-value decomposition of $\mathbf{B}$. Note that in this

formulation, the inverse of $\mathbf{B}$ (or the square root of its inverse) is actually never needed, making it possible to constrain the inversion with a non invertible matrix.

In practice, the preconditioning adds two extra steps to the algorithm described above: conversion from ω to $\mathbf{x}$ ($\mathbf{x} = \mathbf{B}^{1/2}\omega +$
165 $\mathbf{x_b}$) before applying the transport operator (i.e. running the transport model), just before step 1; Conversion from $\nabla_{\mathbf{x}}J_{obs}$ to $\nabla_\omega J_{obs}$ (just after step 2). The initial preconditioned control vector is filled with zeros and corresponds to $\mathbf{x_0} = \mathbf{x_b}$.

3.2 Observation operator (transport model)

The observation operator (H in Equation 2) groups the ensemble of operations to compute the CO_2 concentrations corresponding to a given control vector. In our case, this covers the disaggregation from the monthly fluxes in the control vector to a
170 3-hourly temporal resolution, the addition of prescribed fluxes (fossil, ocean and biomass burning categories), their transport to the observations location and the addition of background concentrations.

In this first implementation of CO_2 inversions with LUMIA, we opted for a regional transport model based on pre-computed observational response functions (footprints):

$$y_m^i = y_{bg}^i + \sum_i \sum_c \langle \mathbf{K_i}, \mathbf{f_c} \rangle \tag{5}$$

175 where the footprint $\mathbf{K_i}$ stores the sensitivity of the observation y^i to the surface fluxes $\mathbf{f_c}$ (with the index c referring to the flux category), and y_{bg}^i is the contribution of background and historical fluxes to the model estimate y_m^i of observation y^i.

The flux vectors $\mathbf{f_c}$ are constructed from the control vector for the optimized flux category (NEE) and prescribed for the other fluxes. The relation between the control vector and the $\mathbf{f}_{nee}$ is given by:

$$\mathbf{f}_{nee}^t = \frac{\mathbf{x}^m - \mathbf{x}_b^m}{n_t} + \mathbf{f}_{0_{nee}}^t$$
$$\mathbf{x}_b^m = \sum_t \mathbf{f}_{0_{nee}}^t \tag{6}$$

180 where $\mathbf{f}_{nee}^t$ is the NEE flux map at time step t of the month m, $\mathbf{f}_{0_{nee}}^t$ is the corresponding prior NEE map, $\mathbf{x}^m$ and $\mathbf{x}_b^m$ are the control vector and prior control vector components corresponding to month m at the same spatial coordinates, and n_t is the number of three-hourly intervals in the month m. In other words, the inversion adjusts an offset to the prior, high temporal resolution fluxes.

The adjoint operations corresponding to Equations 5 and 6 are summarized by

185 $$\mathbf{x}_{adj}^m = \frac{1}{n_t} \sum_t^{n_t} \sum_i \mathbf{K}_i^t \delta y^i \tag{7}$$

with δ_y^i the model-data mismatches weighted by their uncertainties (See Section 3.3.1).

Since $\mathbf{K}$ and y_{bg} are constant throughout the inversion iterations, they can be pre-computed, which reduces the transport computations to a set of very simple matrix operations. This tremendously reduces the computational cost of the inversions but increases the I/O and storage requirements (one response function $\mathbf{K}$ must be stored for each observation and is read at each forward and adjoint iteration).

3.2.1 Response functions (regional transport model)

The response functions ($\mathbf{K}$) were computed using the FLEXPART 10.0 Lagrangian transport model (Seibert and Frank, 2004; Stohl et al., 2010). FLEXPART simulates the dispersion, backwards in time from the observation location, of a large number of virtual air "particles". The response function $\mathbf{K}_i^\phi$ corresponds to the aggregated residence time of the particles released for observation y^i, in a given space-time grid box ϕ of the regional inversion, and below a threshold altitude layer arbitrarily set to 100m).

The simulations were driven by ECMWF ERA-Interim reanalysis, extracted at a 3-hourly temporal resolution, and on a $0.5° \times 0.5°$ horizontal resolution, on a regional domain ranging from $25°W, 23°N$ to $45°W, 83°N$, slightly larger than the inversion grid, which allows for some accounting of particles re-entry (i.e. when an air mass leaves the inversion domain, and re-enters it later, which is not accounted for in the background).

One set of 3-hourly response functions was computed for each observation, up to seven days backward in time (less if all the particles leave the domain sooner). For plain or low altitude sites (see Table 1), the particles were released from the sampling height above ground of the observations. For high altitude sites (around which the orography is unlikely to be correctly accounted for), the particles were released from the altitude above sea level of the observation sites.

The response functions are stored in HDF5 files, following a format described in SI. More detailed information on the configuration of the FLEXPART runs is also provided in SI.

3.2.2 Background concentrations (global transport model)

The background CO_2 concentrations (y^{bg} in Equation 5) result from the transport of CO_2-loaded air masses from outside the regional inversion domain to the observation sites. One approach to compute these background concentrations has been proposed by Rödenbeck et al. (2009), and consists in extracting background concentrations time series at the observation sites from the model output of a global, coarse resolution Eulerian transport model, driven by a set of inversion-derived CO_2 fluxes.

The background extraction is done in three steps:

1. A global, coarse resolution inversion is performed, constrained by a realistic set of prior CO_2 fluxes f_{apri}^{glo}, an initial atmospheric distribution of CO_2 concentrations (C^{ini}), a set of global, background surface CO_2 observations and a subset of the observations to be used later in the regional, high resolution CO_2 inversion. The aim of this step is to obtain a set of CO_2 fluxes f^{glo} that leads to a very realistic atmospheric CO_2 distribution in and around the regional inversion domain (RID). The accuracy of the fluxes themselves has less importance.

2. The CO_2 concentrations y^{tot} corresponding to the transport of the optimized coarse resolution fluxes f^{glo} to the observation sites within the RID are computed using a forward run of the global transport model used in step 1. The foreground CO_2 concentrations y^{fg} are computed using a modified version of that same model, in which the fluxes and concentrations are maintained as zero at all times outside the regional domain, so that the concentrations y^{fg} result only from the transport of the fraction of the fluxes f^{glo} that is within the RID.

3. The background CO_2 concentrations are obtained by subtraction of the foreground concentrations to the total ones ($y^{bg} = y^{tot} - y^{fg}$).

225 The underlying assumptions is, that, by the time the air masses originating from outside the RID reach the observation sites, existing high resolution patterns of CO_2 at the regional domain boundaries concentrations would have been dispersed, and therefore the field of background CO_2 concentrations within the RID can be well represented with a coarse resolution transport model. On the other hand, this background CO_2 distribution should be as realistic as possible (within the limits of the model resolution), especially in and around the boundaries of the foreground domain, therefore the use of an inversion in step 1 above.

230 We refer to Rödenbeck et al. (2009) for a much more complete description of the approach.

We implemented the Rödenbeck et al. (2009) approach in a TM5 model setup (Huijnen et al., 2010) with the initial global inversion (step 1) performed in a TM5-4DVAR setup, based on (Basu et al., 2013a). The NEE flux is optimized monthly on a global $6° \times 4°$ grid, and three additional prescribed CO_2 flux categories are accounted for (fossil fuel, biomass burning and ocean sink). It covers the entire period of the LUMIA inversion, plus six extra months at the beginning and one at the end to

235 limit the influence of the initial condition and to ensure that the background concentrations in the last month of the LUMIA inversion are well constrained by the observations (observations provide important constraints on the fluxes from the preceding month).

The inversion is constrained by flask observations from the NOAA ESRL Carbon Cycle Cooperative Global Air Sampling Network (Dlugokencky et al., 2019) outside the European domain, and by a subset of the observations used for the regional

240 inversion within the European domain (see Section 3.3 for references, and SI for a full list of the sites used in that step).

Since the focus of this inversion is to produce a realistic CO_2 distribution around the European domain, the choice of a prior matters a lot less than the selection of observations. For practical reasons, prior fluxes from the CarbonTracker 2016 release were used (Peters et al., 2007): the NEE prior is generated by the SibCASA model (Schaefer et al., 2008); fossil fuel emissions spatially distributed according to the EDGAR4.2 inventory (https://edgar.jrc.ec.europa.eu/overview.php?v=42);

245 biomass burning emissions are based on the GFED4.1s product (Van Der Werf et al., 2017) and the ocean flux is based on the Takahashi et al. (2009) climatology. We refer to the official CarbonTracker 2016 documentation (https://www.esrl.noaa.gov/gmd/ccgg/carbontracker/CT2016) and to references therein for further documentation on these priors.

The total (y^{tot}) and foreground (y^{fg}) CO_2 concentration time series at the observation sites are extracted using a modified forward TM5 run implementing the step 2 of the background extraction approach described above. The foreground and total

250 CO_2 time series were saved for each observation site, both as continuous (every 30 minutes) concentration time series, sampled at the actual altitude (above sea level) of the observation site, but also as vertical profiles between the surface (as defined in the

TM5 orography) and 5000 m.a.s.l (with a vertical resolution of 250 m and a temporal resolution of 30 minutes). The latter is used to construct a part of the observation uncertainties.

3.3   Observations and observation uncertainties

255   Observations from the GLOBALVIEWplus 4.2 obspack product were used in the inversions (NOAA Carbon Cycle Group ObsPack Team, 2019). For the year 2011, the product includes observations from 26 sites within our regional domain (in addition to observations from mobile platforms, which were not used). Continuous observations are available at 18 of these 26 sites and nine sites are high altitude. Most of these observation sites are now part of the European ICOS network. A list of the sites (coordinates, observation frequency, sampling height and data provider) is provided in Table 1, and the location of the
260   observations is also reported in Figure 2.

3.3.1   Observation uncertainties

The observation uncertainty matrix ($\mathbf{R}$) accounts for both the measurement uncertainties (ε_{obs}) and the model representation uncertainty (ε_H, i.e. the incapacity of the model to represent perfectly well the observations, even given perfect fluxes). In theory, the diagonal of the matrix stores the absolute total uncertainty associated to each observation while the off-diagonals
265   should store the observation error correlations. In practice, these correlations are difficult to quantify, and the size of the matrix would anyway make it impractical to invert. The off-diagonals are therefore ignored in our system (as in most similar inversion setups) and the observation uncertainty is stored in a simpler observation error vector, ε_y.

Our inversion system uses an observation operator that decomposes the background and foreground components of the CO_2 mixing ratio, therefore the model uncertainty can itself be decomposed in foreground and background uncertainties:

$$270 \quad \varepsilon_y = \sqrt{\max\{\varepsilon_{obs}, \varepsilon_{obs}^{min}\}^2 + \varepsilon_{bg}^2 + \varepsilon_{fg}^2} \qquad (8)$$

The instrumental error (ε_y) is provided by the data providers for most of the observations, and typically ranges between 0.1-0.7 ppm (see Figure 3). We enforced a minimum instrumental error (ε_{obs}^{min}) of 0.3 ppm for all the observations.

The model representation error can not be formally quantified, as this would require knowing precisely the CO_2 fluxes that the inversion is attempting to estimate. One can, however, assign representation error estimates (foreground and background)
275   based, in particular, on assumptions of situations that would normally lead to a degradation of the model performances (for instance late-night/early-morning observations, with a development of the boundary layer that may not be well captured by the model, or observations in regions with a complex orography). Transport model comparisons can also provide representation error estimates based on the difference in their results.

3.3.2   Foreground model uncertainties:

280 As described in Section 3.2.2, background and foreground CO_2 concentrations are computed for each observation site from a TM5 simulation. We performed a forward transport simulation with the regional transport model in LUMIA, using both the background concentrations and the foreground fluxes from that TM5 simulation, so that the two simulations differ only by their regional transport model. A comparison between the concentrations computed by the two models is shown in Figure 4. The bias between the two models is very contained during the summer months (it is below 0.2 ppm from April to September,

285 and goes as low as 0.01 ppm in July), but rises during the winter months (up to 1.45 ppm in November). The mean average difference between the two simulations is also much larger in winter: it ranges from 0.82 ppm in September to 4.3 ppm in November, with a yearly average of 3.3 ppm.

This comparison is not a formal performance assessment of either TM5 or of the FLEXPART-based transport used in LUMIA, and it particular the bias should be interpreted with care as the sign of the total net foreground flux changes during

290 the year (which mechanically leads to a change of the sign of the bias). Nonetheless, it provides an indication on the order of magnitude of the foreground model transport errors. We use the absolute differences between the two models as a proxy for ε_{fg}.

3.3.3   Background model uncertainties:

Background concentrations are expected to be accurately estimated by the global TM5 inversion when the dominant winds

295 are from the West and that any signal from a strong point CO_2 source or sink has had time to dissipate along the air mass trajectory over the Atlantic Ocean. In less favourable conditions, there can be entries of less well-mixed air inside the domain, in particular in case of Easterly winds or in events of re-entry of continental air that would have previously left the domain. These events are less likely to be well captured by the TM5 inversion and should be attributed a higher uncertainty.

There is no perfect and easy way to detect these events, but one of their consequences would be a less homogeneous

300 background CO_2 distribution around the observation sites when they occur. As part of the TM5 simulation, vertical profiles of background concentrations were stored for each observation (from the surface to 5000 m.a.s.l, at a 250m vertical resolution). We set the background uncertainty of each observation (ε_{bg}) to the standard deviation of its corresponding background CO_2 vertical profile. ε_{bg} is on average 0.36 ppm, one order of magnitude lower than ε_{fg}, and it is also more constant (it ranges between 0.01 and 3.6 ppm). Note that these statistics are computed before the observation selection procedure, described in

305 the following section. The different components of the observation uncertainty are compared in Figure 3 for two representative sites.

3.3.4   Observation selection

The inversions are performed on a subset of the observations included in the obspack product. Only observations for which the transport model simulation is expected to result in accurate concentrations are kept. In practice, one of the main difficulties of

310 transport modelling is to correctly compute the mixing of air in the lower troposphere below the boundary layer. The lowest
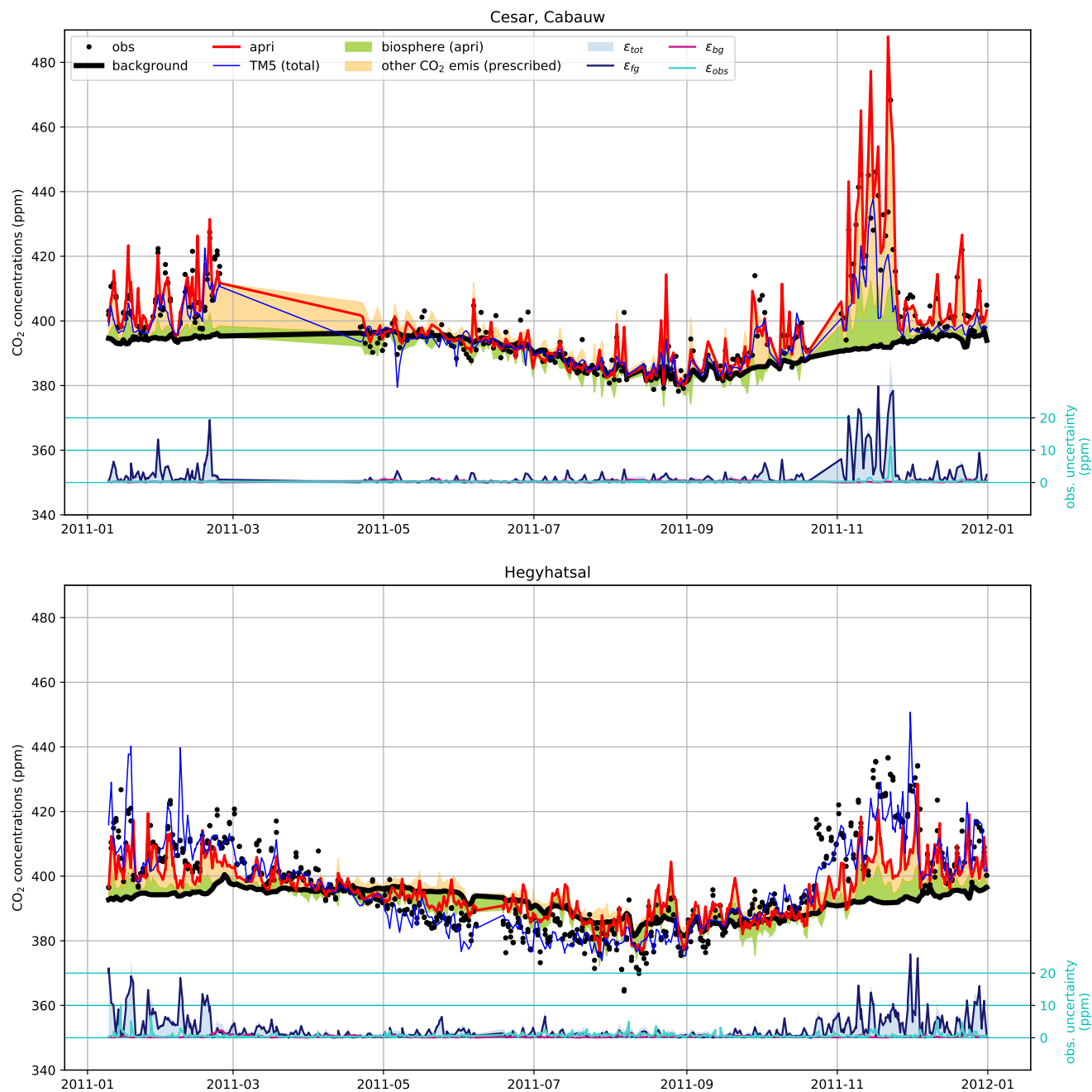
Figure 3. Decomposition of the modelled mixing ratio and of the observation uncertainties at two sites (Cabauw, The Netherlands and Hegyhatsal, Hungary). The "TM5 total" line is the concentration computed in the coarse resolution TM5 inversion from which the background (thick black line) is extracted. The LUMIA prior concentration is shown in red and the green and orange shaded areas show respectively the contribution of the prior biosphere flux and of the other CO_2 fluxes to the difference between that prior and the background. The lower series of lines in each plot (with y-axis on the right) shows the total observation uncertainty (blue shaded area), and the contributions of the foreground, background and observational uncertainties.
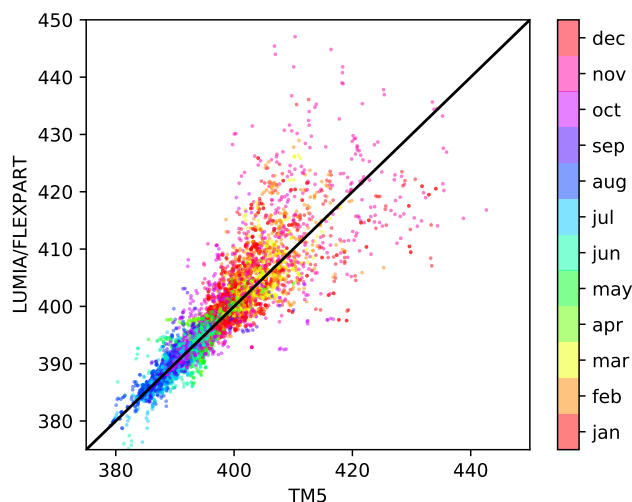
Figure 4. LUMIA (CO_2 concentrations obtained with TM5-FLEXPART vs. with TM5, using the CO_2 fluxes used as prior of the TM5 inversion (background). The color of the dots show the observation month.

model representation error is expected for observations that are either within the boundary layer when it is most developed (in the afternoon), or well above the boundary layer for high-altitude sites (during the night). For each site with continuous observations, we selected only observations sampled during the time range for which the model is expected to perform the best. The time ranges are based on the "`dataset_time_window_utc`" flag in the metadata of the observation files from

315   the obspack. For sites with discrete sampling, all observations were used.

A second filter, used in some of the inversions and in the background TM5 inversion (Section 3.2.2), is the limitation of a maximum of one observation per 24 hours at each observation site (the one that has the lowest observation uncertainty, as per the definition in the previous above). This is justified by the fact that two observations at a same site, within a small time interval have strongly correlated model representation errors and do therefore not provide independent information. In the absence of

320   a proper accounting of observational error correlations, it may be preferable to limit the number of assimilated observations. The use of this second observation filter is discussed in further details in Section 5.

3.4   Prior and prescribed fluxes

In addition of the Net Ecosystem Exchange (NEE, net atmosphere-land CO_2 flux) that is optimized in the inversions, the simulations also account for anthropogenic CO_2 emissions (combustion of fossil fuels, bio fuels and cement production), for

325   biomass burning emissions (large scale forest fires) and for the ocean-atmosphere CO_2 exchanges.

The NEE prior is taken from simulations of the LPJ-GUESS and ORCHIDEE vegetation models: in the OSSEs (Section 4) ORCHIDEE fluxes are used as prior and LPJ-GUESS fluxes are used as truth, while in inversions against real data LPJ-GUESS fluxes are used as prior. Both vegetation models provide 3-hourly fluxes, on a horizontal $0.5° \times 0.5°$ grid.

Code	Name	Lat (°E)	Lon (°N)	Alt (m.a.s.l)	Intake Height (m.a.g.l)	Nobs	Time range (h)	sets	Data provider
BAL	Baltic Sea	55.35	17.22	3	25	53	all	P	1
BSC	Black Sea, Constanta	44.18	28.66	0	5	17	all	P	1
CES200	Cesar, Cabauw	51.97	4.93	-1	200	306	11-15	P	2
CIB005	Centro de Investigacion de la Baja Atmosfera (CIBA)	41.81	-4.93	845	5	49	*	A	1
CMN	Mt. Cimone Station	44.18	10.70	2165	12	549	23-3	A	3
CRP	Carnsore Point	52.18	-6.37	9	14	589	12-16	P	4
ELL	Estany Llong	42.57	0.95	2002	3	8	11-15	A	5
HEI	Heidelberg	49.42	8.67	116	30	632	11-15	P	6
HPB054	Hohenpeissenberg	47.80	11.02	936	54	47	all	A	1
HUN115	Hegyhatsal	46.95	16.65	248	115	685	11-15	P	7
JFJ	Jungfraujoch	46.55	7.99	3570	10	461	23-3	A	8
KAS	Kasprowy Wierch	49.23	19.98	1989	5	481	23-3	A	9
LMP005	Lampedusa	35.52	12.62	45	5	35	all	P	1
LMP008	Lampedusa	35.52	12.62	45	8	418	10-14	PA	10
LUT	Lutjewad	53.40	6.35	1	60	289	11-15	P	11
MHD024	Mace Head	53.33	-9.90	5	24	352	12-16	P	12
OPE120	Observatoire Perenne de l'Environnement	48.56	5.50	390	120	405	11-15	P	12
OXK163	Ochsenkopf	50.03	11.81	1022	163	48	all	A	1
PAL	Pallas-Sammaltunturi	67.97	24.12	565	5	654	22-2	PA	13
PRS	Plateau Rosa Station	45.93	7.70	3480	10	445	23-3	A	14
PUI	Puijo	62.91	27.65	232	84	170	11-15	P	13
PUY010	Puy de Dome	45.77	2.97	1465	10	409	23-3	A	12
PUY015	Puy de Dome	45.77	2.97	1465	15	141	23-3	A	12
SSL	Schauinsland	47.92	7.92	1205	12	625	23-3	A	15
TRN180	Trainou	47.96	2.11	131	180	539	11-15	P	12
TTA	Tall Tower Angus	56.56	-2.99	400	222	435	12-16	PA	16
WAO	Weybourne, Norfolk	52.95	1.12	20	10	1078	12-16	P	17
WES	WES	54.93	8.32	12	0	1377	11-15	P	18

Table 1. Observation sites used in the inversions. The Data providers: 1:NOAA Carbon Cycle Group ObsPack Team (2019); 2:Vermeulen et al. (2011); 3:Ciattaglia et al. (1987); 4:D. Dodd (EPA Ireland); 5:J.A. Morgui and R. Curcoll (ICTA-UAB, Spain); 6:Hammer et al. (2008); 7:Haszpra et al. (2001); 8:Uglietti et al. (2011); 9:Rozanski et al. (2014); 10:A. G. di Sarra (ENEA, Italy); 11:van der Laan et al. (2009); 12:Yver et al. (2011); 13:Hatakka et al. (2003); 14:F. Apadula (RSE, Italy); 15:Schmidt (2003); 16:Ganesan et al. (2015); 17:Wilson (2012); 18:K. Uhse (UBA, Germany)

330   LPJ-GUESS (Smith et al., 2014) is a dynamic global vegetation model (DGVM), which combines process-based descriptions of terrestrial ecosystem structure (vegetation composition, biomass and height) and function (energy absorption, carbon and nitrogen cycling). The vegetation is simulated as a series of replicate patches, in which individuals of each simulated plant functional type (or species) compete for the available resources of light and water, as prescribed by the climate data. The model is forced using the WFDEI meteorological data set (Weedon et al., 2014) and produces 3-hourly output of gross and net carbon fluxes.

Category	Product	Original resolution	Data provider	Total (min/max) flux (PgC/year)
Biosphere	LPJ-GUESS	$0.5° \times 0.5°$; 3-hourly	Lund University	-0.33 (-2.65 / 1.85)
Biosphere	ORCHIDEE	$0.5° \times 0.5°$; 3-hourly	LSCE (P. Peylin, pers. comm)	-0.28 (-3.73 / 2.14)
Fossil	EDGARv4.3	$0.1° \times 0.1°$; hourly	ICOS-CP + JRC	1.53
Ocean	CarboScopev (oc_v1.7)	$5° \times 3.83°$; daily	Rödenbeck et al. (2013)	-0.11 (-0.05 / 0.01)
Fires	GFEDv4	$0.5° \times 0.5°$; 3-hourly	Van Der Werf et al. (2017)	0.01

Table 2. Prior and prescribed CO_2 fluxes. Min/Max values are provided for the fluxes that have both positive and negative components, and correspond to the minimum and maximum values of the 3-hourly flux aggregated over the entire domain, in PgC/year.

335   ORCHIDEE is a global processed-based terrestrial biosphere model (initially described in Krinner et al. (2005)) that computes carbon, water and energy fluxes between the land surface and the atmosphere and within the soil-plant continuum. The model computes the Gross Primary Productivity with the assimilation of carbon based on the Farquhar et al. (1980) for C3 plants and thus account for the response of vegetation growth to increasing atmospheric CO_2 levels and to climate variability. The land cover change (including deforestation, regrowth and cropland dynamic) were prescribed using annual land cover

340   maps derived from the Harmonized land use data set (Hurtt et al., 2011) combined with the the ESA-CCI land cover products. The net and gross CO_2 fluxes used for this project correspond to the one provided for Global Carbon Project inter-comparison (Le Quéré et al., 2018) with a model version that was updated recently (Peylin et al., in preparation).

   Fossil fuel emissions are based on a pre-release of the EDGARv4.3 inventory for the base year 2010 (Janssens-Maenhout et al., 2019). This specific dataset includes additional information on the fuel mix per emission sector and thus allows for

345   a temporal scaling of the gridded annual emissions for the inversion year (2011) according to year-to-year changes of fuel consumption data at national level (bp2, 2016), following the approach of Steinbach et al. (2011). A further temporal disaggregation into hourly emissions is based on specific temporal factors (seasonal, weekly, and daily cycles) for different emission sectors (Denier van der Gon et al., 2016).

   The ocean-atmosphere flux is taken from the Jena CarboScope v1.5 product, which provides temporally and spatially re-

350   solved estimates of the global sea-air CO_2 flux, estimated by fitting a simple data-driven diagnostic model of ocean mixed-layer biogeochemistry to surface-ocean CO_2 partial pressure data from the SOCAT v1.5 database (Rödenbeck et al., 2013).

   A biomass burning flux category was also included in the inversion, based on fluxes from the Global Fire Emission Database v4 (Giglio et al., 2013). In our European domain biomass burning emissions are negligible regarding the other CO_2 emission sources, however, we include it for completeness.

355   All fluxes are regridded on the same $0.5° \times 0.5°$, 3-hourly resolution (by simple aggregation or re-binning). A summary of the prior fluxes sources, original resolution and yearly totals is provided in Table 2.

3.4.1 Prior uncertainties

The background error covariance matrix ($\mathbf{B}$ in Equation 2) is constructed following the "correlation length" approach used in many other inversion systems (e.g. Houweling et al. (2014); Thompson et al. (2015); Chevallier et al. (2005)): The error

360 covariance between fluxes $\mathbf{x_1}$ and $\mathbf{x_2}$ at gridcells with coordinates $p_1 = (i1, j1, t1)$ and $p_2 = (i2, j2, t2)$ is defined as:

$$cov(\mathbf{x_1}, \mathbf{x_2}) = \sigma^2_{\mathbf{x_1}} . \sigma^2_{\mathbf{x_2}} . C_h(p_1, p_2) . C_t(p_1, p_2) \qquad (9)$$

where $\sigma^2_{\mathbf{x_1}}$ and $\sigma^2_{\mathbf{x_2}}$ are the variances assigned to the prior monthly NEE at coordinates p_1 and p_2, and C_h and C_t are decay functions of the spatial (C_h) and temporal (C_t) distance between p_1 and p_2, defined respectively as $C_t(p_1, p_2) = e^{-|t_1 - t_2|/L_t}$ and $C_h = e^{-\left(\frac{d(p_1, p_2)}{L_h}\right)^{\beta}}$, with $d(p_1, p_2)$ the geographic distance between the center of the two pixels. L_t and L_h are temporal

365 and spatial correlation length. The decay functions are further referred as Gaussian or exponential decay functions, depending on the value of the β parameter (1 for exponential, 2 for Gaussian). We explore the two versions of decay functions in our OSSEs described in Section 4.

The true uncertainty of the prior fluxes ($\sigma^2_{\mathbf{x}}$) is difficult to evaluate and is therefore constructed on reasonable but arbitrary assumptions. We assumed that the flux uncertainties scale linearly with the net flux, and therefore to set the individual flux

370 uncertainties to a constant fraction of the absolute net flux, possibly within a range.

This approach is practical as is doesn't require any additional inputs, and justified by the fact that the uncertainties should be low in areas where the flux is known to be low (for instance, desert areas in a CO_2 inversion). One drawback however is that the net CO_2 flux (NEE) may be close to zero as a result from the gross fluxes (GPP and respiration) of same magnitude. An alternative approach is setting the uncertainty as a scaling factor of the vegetation respiration. We did not explore this here

375 because of a lack of a respiration field at the beginning of the study.

4 OSSEs

Simulation	Prior	Observations	$\sigma^2_{\mathbf{x}}$	L_h	L_t
SRef	ORCHIDEE	Truth + $N(\sigma^2_y)$	25% of monthly prior	200 km (exp)	1 month
SB	-	Truth + R + B	-	200 km (exp)	-
S500	-	Truth + R	-	500 km (exp)	-
S100	-	Truth + R	-	100 km (exp)	-
SG	-	Truth + R	-	200 km (gauss)	-
SP	-	Truth (set P) + R	-	200 km (exp)	-
SA	-	Truth (set A) + R	-	200 km (exp)	-
RRef	LPJ-GUESS	Real	25% of monthly prior	200 km (gauss)	1 month
R500	-	Real (set P)	-	500 km (gauss)	-
R100	-	Real (max 1 obs/24h/site)	-	100 km (gauss)	-
RP	-	Real (set A)	-	200 km (gauss)	-
RA	-	Real	-	200 km (gauss)	-
Rlf	-	Real	-	200 km (gauss)	

Table 3. List of inversion experiments performed. The R and B letters in the Observations column refer respectively to a random error perturbation (R, proportional to the assigned individual uncertainty of each observation) and to a systematic bias (B), described in the main text of Section 4. The restricted observation sets A and P are reported in Table 1.

A series of OSSEs was performed aiming primarily at verifying the absence of abnormal behaviour of the inversion system (i.e. verify that it converges towards the truth and responds as expected to changes in observational or prior constraints). The OSSEs share a common prior NEE (ORCHIDEE) and a common set of observations derived from a forward propagation of the "true" (LPJ-GUESS) fluxes (at the same time and location as the actual observations listed in Table 1), perturbed by a random

380 error ($y = y^{truth} + \mathcal{N}(0, \sigma_y^2)$, with σ_y^2 the uncertainty of each observation as defined in the matrix $\mathbf{R}$).

In the reference inversion Sref, the prior error covariance matrix ($\mathbf{B}$) is constructed with prior uncertainties set to 25% of the absolute prior value ($\sigma_{\mathbf{x_b}}^2 = 0.25|\mathbf{x_b}|$) and exponentially decaying horizontal and temporal covariances, with a horizontal covariance length (L_h) of 200 km and a temporal covariance length (L_t) of one month.

385 Inversions S500 and S100 differ from Sref by the use of respectively longer (500 km) and shorter (100 km) horizontal covariance lengths. Inversion SG uses a Gaussian decay function instead the of exponential one used in Sref. Inversions SP and SA use respectively only the low altitude and only the high altitude sites (See Table 1). Inversion SB is similar to Sref but uses a perturbed set of background CO_2 concentrations: $y_{pert}^{bg} = 0.75 y_{truth}^{bg} + 0.25 y_{prior}^{bg}$, with y_{prior}^{bg} the background concentrations corresponding to the prior fluxes of the coarse resolution TM5 inversion from which y_{truth}^{bg} are generated (See Section 3.2.2).

390 ## 4.1 Domain-wide NEE budget

The net annual budget is one of the first quantities typically looked at in an atmospheric inversion. The net annual NEE optimized in the six OSSEs are compared to the prior and true NEE in the upper panel of Figure 5. At this annual scale, all the inversions degrade the flux estimate. Most inversions point to a near zero annual flux (from -0.04 PgC/year in S100 to -0.1 PgC in SP and S500. SB is the closest to the 'true' flux, despite being constrained by biased background concentrations, with

395 annual estimate of -0.4 PgC/year (20% larger than the 0.33 PgC/year of the synthetic truth).

On the other hand, the lower panel of Figure 5 compares the root mean square error of the inversions to that of the prior: all the inversions lead to a reduction of the RMSE by ≈30%. Inversion S100 performs marginally better, and SP and SG marginally worse.

These contradictory analyses can be explained by looking at the fluxes at the monthly scale, shown in the upper panel of

400 Figure 5. The prior NEE has a much more pronounced seasonal cycle than our assumed truth. The summer uptake is, for instance, almost three times larger in the prior and the winter release of carbon to the atmosphere is also much stronger than in the 'true' fluxes.

At the domain scale, all the inversions are able to bring the prior seasonal cycle in agreement with the one imprinted in the pseudo-observations, although performances differ slightly. Most of the time, inversion S500 leads to the most accurate

405 representation of the true NEE, with a net error in a ±0.05 PgC/month range. By comparison, inversion SB leads to similar performances in winter (August to April), but does not achieve the same error reduction in summer, with a net monthly summer error in a -0.11 to -0.15 PgC/month range from May to July. The better performance of inversion SB in estimating the annual budget of NEE is explained by errors of opposite sign in summer and winter, compensating each other. More generally, the differences between the optimized annual budgets shown in Figure 5 are explained by errors of opposite sign, more or less

410 compensating each other, and are not a good indication of the inversions performance.
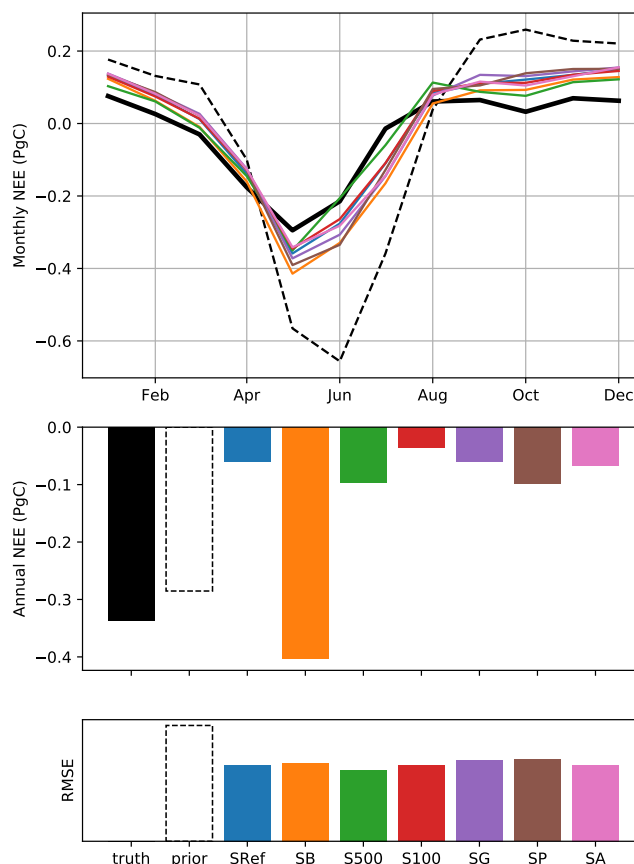
Figure 5. Top: Monthly prior (dashed black line), true (thick solid black line) and posterior NEE aggregated on the whole inversion domain; Middle: Annual NEE budgets (truth, prior and posteriors); Bottom: RMSE (with respects to the arbitrary truth).

4.1.1 Regional decomposition

Aggregated monthly and annual regional totals are shown for all the inversions in Figure 6 (with the region definitions provided in SI). The bar plots on the left show the prior, true and posterior annual NEE budgets in each region, and the plots on the right show the monthly prior and posterior differences with the "true" regional NEE.

415   As it is the case at the domain-scale, the monthly regional NEE budgets are systematically improved by the inversions. This sometimes leads to degradation of the representation of the annual budget (in the Northern, Southern and Eastern Europe regions in particular), which confirms that the annual budget is not robustly constrained by our system, contrarily to the monthly NEE.

    The largest discrepancies are found in the Eastern, Northern and South-Eastern Europe regions, where the observation
420   network is the densest. On the other hand, the flux estimate is, at least at the monthly scale, very insensitive to the different

inversion settings in Central Europe. Reductions in the network density only leads to marginal degradation of the monthly regional NEE (at least in these large regions).

The use of a biased set of background concentrations in inversion SB affects the Western Europe region more than any other: background air generally enters the domain from the West, and Western Europe fluxes are then used as a buffer to compensate

425   for this biased background.

Inversion S500 behaves noticeably different from the other inversions in Northern, Eastern and South-Eastern Europe (the three regions that are the least constrained by observations): Inversion S500 uses longer spatial covariance lengths (500 km). Therefore, the flux adjustments will be spread over a larger area than in e.g. Sref (which uses a **B** matrix constructed by using 200 km covariance lengths). Since the prior error (i.e. the difference between ORCHIDEE and LPJ-GUESS) follows a

430   relatively homogeneous pattern, S500 effectively produces a better estimation of the NEE in Eastern Europe. There is, however, no guarantee that such a conclusion would apply to an inversion constrained by real observations, as the difference between the prior and the real NEE fluxes may not follow such a simple pattern.

This point is further illustrated in Figure 7, which shows maps of prior, posterior (Sref) and true fluxes, and the associated errors and error corrections, for the four seasons. Flux error reductions are more consistently obtained in Eastern and Southern

435   Europe, where the network is the least dense. One straightforward explanation is that the prior errors are much larger in these regions and therefore easier to reduce. But in Western and Central Europe, where the observation network is dense and where neighbour sites occasionally provide contradictory signals, the inversions have to apply more complex corrections to the control vector, which is more difficult when the covariances lengths are long (i.e. in S500) and occasionally leads to locally increased error.

440   **4.2   Evolution of the fit to observations**

The comparison of the prior and posterior model fit to observations is a classical diagnostics of atmospheric inversions (Michalak et al., 2017). The inversion is expected to improve the overall fit to the observation ensemble, and a lack of statistical improvement would generally be a sign of a malfunctioning inversion algorithm. At a finer scale, analysis of the when and where the representation of the observations is most improved (or degraded), can provide useful insights on the performances

445   of the inversion (adequacy of the definition of uncertainties) and on those of the underlying transport model.

In the right panel of Figure 8, we compare the statistical distribution of prior and posterior observation fit residuals for inversion Sref. The plot confirms that the inversion leads to an overall improvement of the representation of observations, albeit modest (prior bias (model-obs): 0.2 ppm; posterior bias: 0.05 ppm; prior RMSE: 4.9 ppm; posterior RMSE: 3.75 ppm).

The left panel shows the RMSE reduction at each observation site for inversion Sref (the size of the dots is proportional to

450   the number of assimilated observations at each site, and the color shows the net RMSE reduction). At all sites the inversion leads to improvements in the fit, but those are generally much more modest in Western Europe.

Finally, the center panel compares the RMSE reduction of inversion Sref to that of the other OSSEs: The best performance is logically achieved by inversion S1 at most of the sites because it is constrained by exact concentrations, and therefore it is easier for the inversion to find a solution. But overall the inversion performances are very comparable.
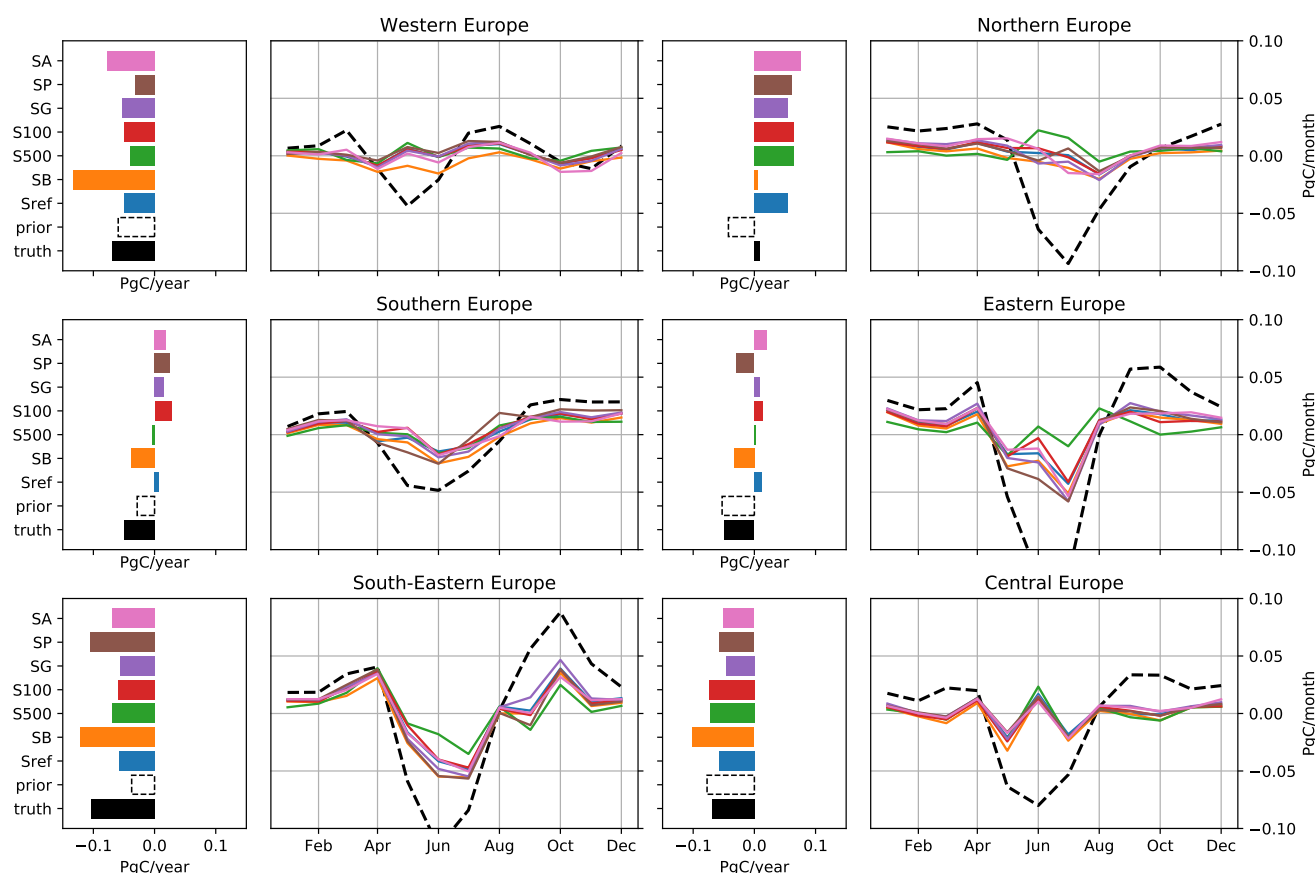
Figure 6. Prior, true and posterior annual regional NEE balance (bar plots) and monthly regional NEE error in the prior and posterior fluxes (line plots)

The comparatively low misfits in continental Europe can be explained by the (coincidental) good performance of the prior in that region (see previous section and Figure 6), but also by the strong sensitivity of these sites to background concentrations. Sites in the UK and, in particular, Ireland sample very little continental air, which leaves little margin for the inversion to improve the representation of their observations.

5 Inversions against real observations

The OSSEs presented above neglect several complications of real inversions, in particular transport model errors (the observations were generated using the same transport model than the one used in the inversions). Quantifying precisely the impact of such transport model errors is not the scope of this paper. Nonetheless, we present results from a set of inversions similar to the OSSEs of Section 4 but constrained by real observations. The objectives are to verify the stability of the solution with
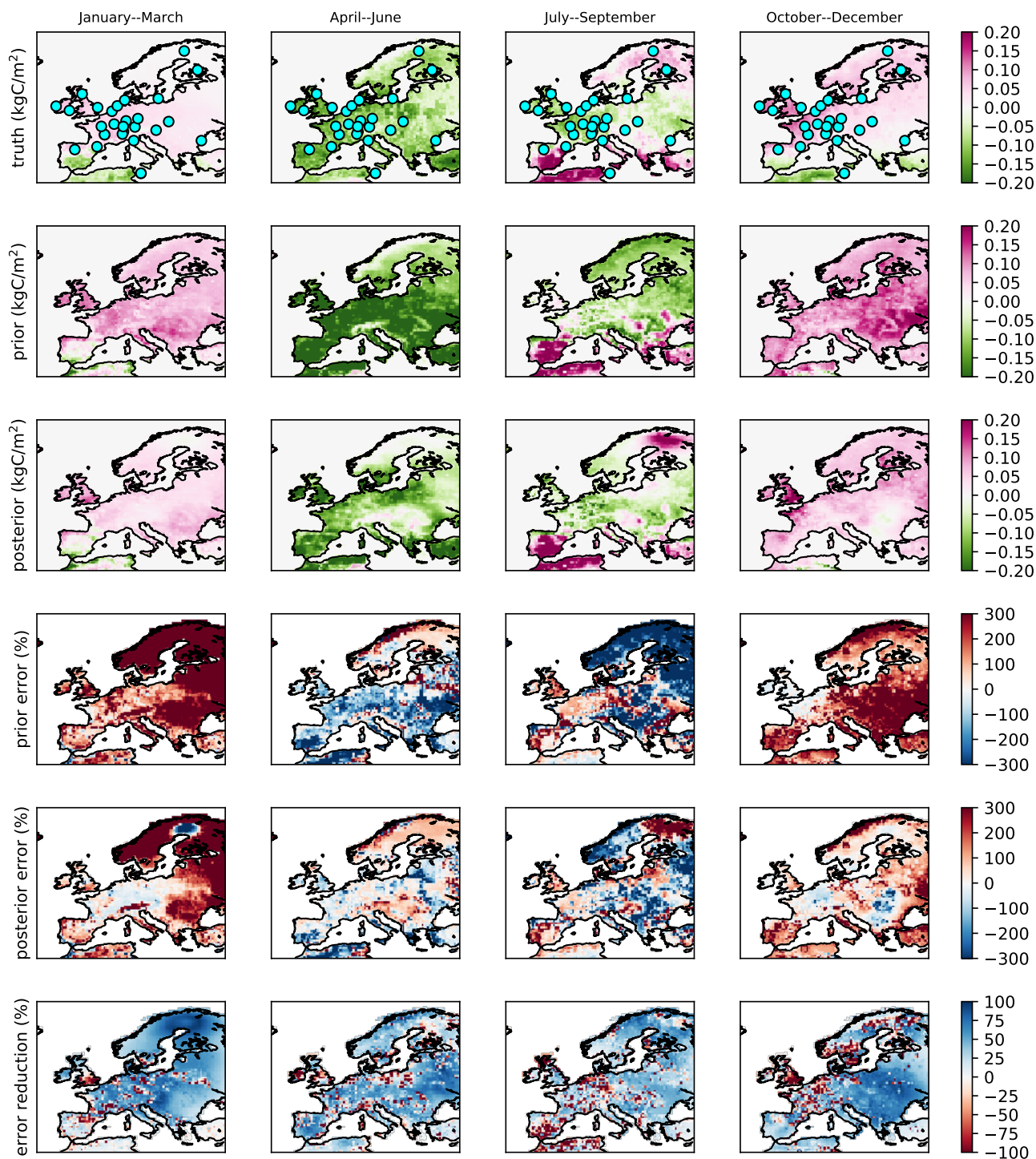
Figure 7. From top to bottom: True fluxes (LPJ-GUESS), prior fluxes (ORCHIDEE), posterior fluxes (inversion S2), relative prior error (in percentage of the true fluxes), relative posterior error and relative error reduction. Each column corresponds to three months (sums for the fluxes and averages for the error and error reductions). The cyan dots show the location of the observation sites.

Geoscientific
Model Development
Discussions
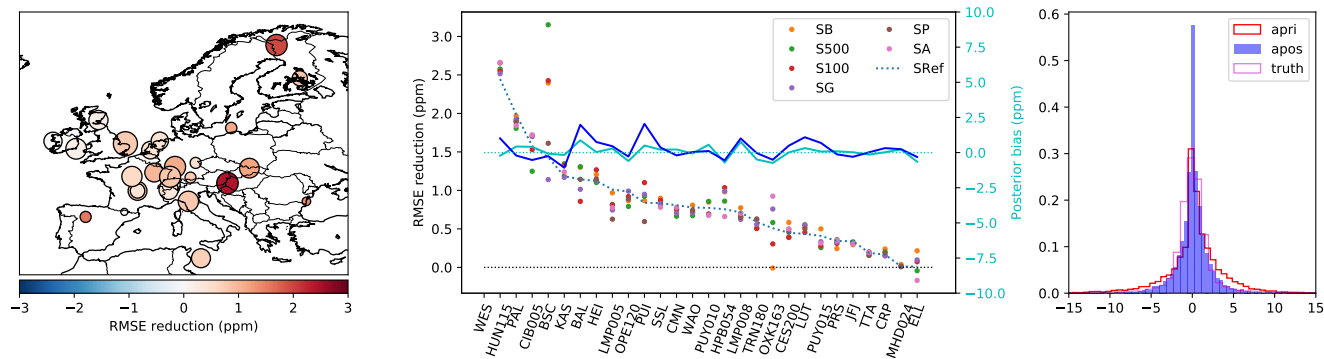
Figure 8. Left: Map of the observation sites in Sref, with the area of the dots proportional to the number of assimilated observation at each site, and the color proportional to the RMSE reduction (prior RMSE minus posterior RMSE). Center: RMSE reduction at each site, for the five sensitivity OSSEs. Right: Prior and posterior distribution of the observation mismatches in Sref (irrespective of the site). The cyan and blue line plots in the center plot show the prior (blue) and posterior (cyan) mean biases at each site (right axis)

.

regards to typical user choices, such as the selection of observations and the definition of prior uncertainties, and to provide
465 some indicators of the transport model performance.

The reference inversion (Rref) is constrained by the observations presented in Section 3.3 and uses a prior terrestrial flux from the LPJ-GUESS model described in Section 3.4. The prior uncertainties ($\sigma^2_{\mathbf{x_b}}$) are set to 25% of the net monthly flux in each pixel, and gaussian spatial correlation length of 200 km and exponential temporal correlation lengths of one month are used. Besides Rref, two groups of inversions were performed (with the specific settings listed in Table 3):

470 – The sensitivity of the fluxes to the observation selection is tested in experiments RP, Rlf and RA. In RP, high altitude sites (see Table 1) have been excluded from the inversion. In Rlf the same observation network as in Rref has been used, but the frequency of observations has been limited to a maximum of one for each day and site. Finally, in RA only high altitude sites plus LMP, PAL and TTA have been used (because of the lack of any altitude site in the regions of these three sites).

475 – Inversions R500 and R100 were designed to assess the impact of the structure of the prior covariance matrix on the results. In inversions R500 and R100, the spatial correlation length used to build **B** was changed to 500 km and 100 km

As for the OSSEs, we analyze first the optimized fluxes and then the evolution of the fits to the observations. Note that this time the true fluxes are not known.

5.1 Optimized fluxes

480 Optimized fluxes are shown in Figure 9, as monthly (left) and annual totals (right), aggregated on the entire domain (first row) and in smaller regions (following the same region definitions used for the OSSEs in Section 4.1.1). At the domain scale, the number of observations has the largest impact on the posterior flux. While the three inversions that use the full dataset

(Rref, R500, R100) find a 50 to 60% reduction of the net NEE sink, inversions RP (which uses only low altitude sites) and Rlf (which uses the same number of sites but a reduced number of observations) lead only to a 25% reduction of the net

485 sink, and RA (altitude sites only) does not adjust the total flux significantly. Focusing on the monthly totals, the inversions consistently point to a larger seasonal cycle than simulated by the LPJ-GUESS model, with a more positive NEE in the winter and autumn months (especially in March, September, October and November), and a stronger carbon uptake in the European summer months. Especially the near-zero NEE in August is clearly contradicted by all the inversions.

The regional decomposition shows a more complex picture. The increased early summer (May-July) uptake is largely at-

490 tributed to three regions: Northern, South-Eastern and Central Europe, and the August shift towards negative NEE is almost entirely due to adjustments in the Southern and Northern Europe regions. On the contrary, the NEE is corrected towards more positive values (reduced uptake in summer and increased release in winter) most of the year (except in May) in Western Europe (and more prominently so in the summer and fall months). In fall and winter CO_2 fluxes to the atmosphere are increased in most of the regions, except in Northern Europe where it is reduced in the fall and unchanged in winter (January to April).

495 Contrarily to what happened in the OSSEs, the spread of the inversions ensemble is not narrower where the network density is the highest. The results in Central Europe are on the contrary extremely sensitive to the restriction of the observation ensemble to high (RA) or low (RP) altitude sites, and changes in the observation frequency (Rlf) also have an impact (but in a predictable sense: they lead to a correction of the flux of smaller amplitude than e.g. Rref). Changes in the spatial covariance lengths (Rref, R500, R100) correspond roughly to what was seen with the OSSEs: the impact is mostly in regions with low observational

500 coverage.

Maps of prior and posterior fluxes are shown in the upper and central row of Figure 10 for the reference inversion Rref. While at large scales the inversion preserves relatively well the spatial NEE distribution, it tends to concentrate a large part of the flux adjustments around some of the observation sites, in particular in Western and Central Europe. On the contrary, flux adjustments are relatively smooth in areas at the domain edges.

505 The lower row of Figure 10 shows the standard deviation of the ensemble at each pixel (and for each 4-month period). The largest discrepancies between the inversions are found around Northern Germany and Poland (in the "Central Europe" region). One likely explanation is site-specific transport model errors: Observations from two sites sensitive partly to the same fluxes, but affected by different systematic model error (biases) may provide apparently contradictory information on the direction and/or amplitude of the flux adjustments. The inversion can only reconcile such contradictory observational information by

510 clustering strong flux adjustments in small areas and/or time periods. The problem is stronger where the network density is the highest, and the ensemble spread varies the most where the network density is the most impacted by the sites selection in inversions RA and RP. In the OSSEs, similar changes in network density did not lead to similar problem because of the use of a perfect transport model.

5.2 Reduction of the observation misfits

515 The comparison of prior and posterior fit residuals is more critical in this series of inversions than in the OSSEs since here the true fluxes are not known. Figure 11 shows observation fits for the R-denoted series of inversions in a similar way than done in
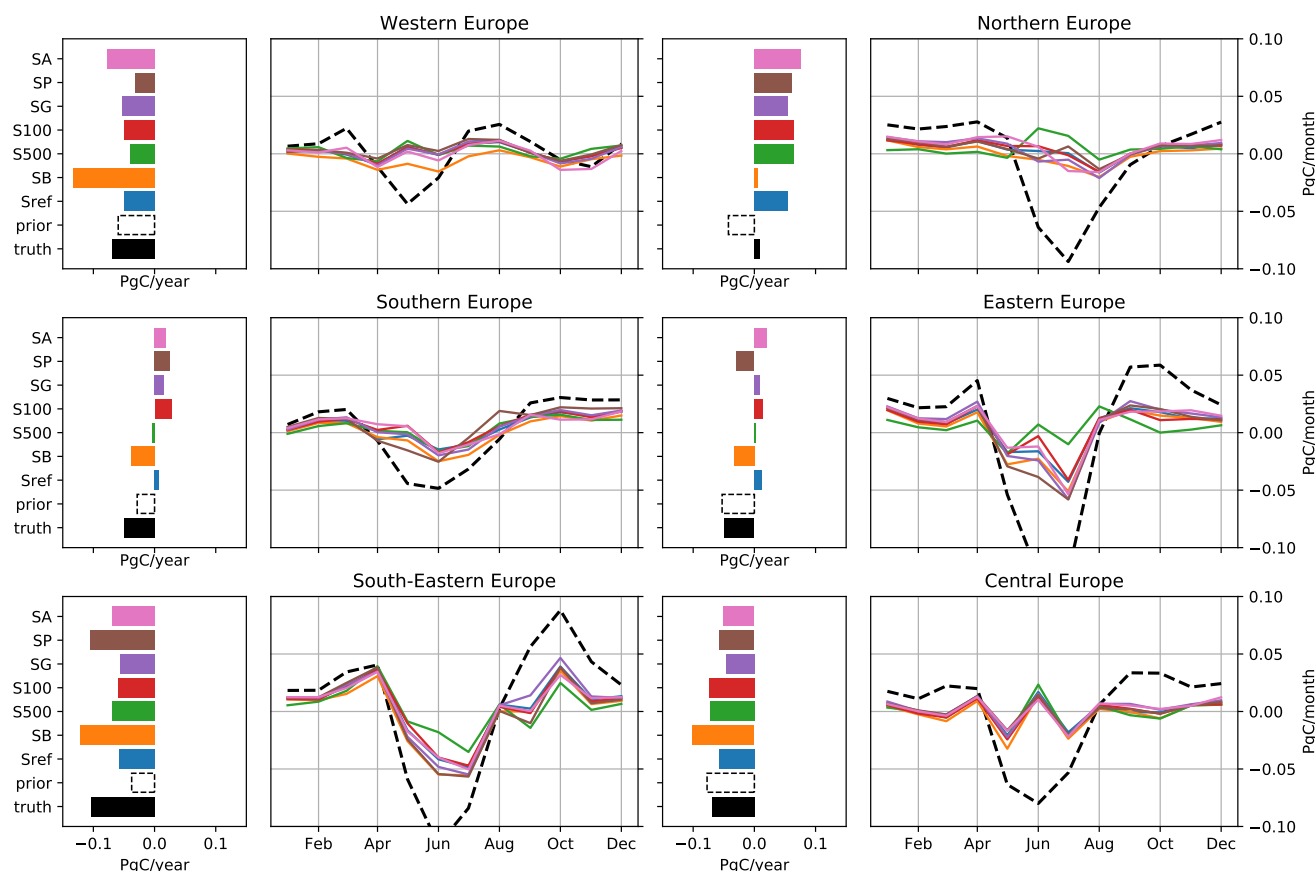
Figure 9. Annual (bar plots) and monthly (line plots) prior and posterior fluxes aggregated on the entire domain (upper row) or in smaller regions.

Section 4.2 for the OSSEs. The overall change in the fit to the observations (right hand panel) from prior to posterior is still an improvement, but this time very modest (mean prior bias: 0.75 ppm; mean posterior bias: -0.03 ppm; prior RMSE: 5.74 ppm; posterior RMSE: 5.40 ppm).

Looking at each site separately (left and middle panels) shows, that, while at most sites the representation of the observations is improved by the inversion (red circles), it is strongly degraded at two sites: OXK (-1.15 ppm) and OPE (-0.74 ppm). At another six sites, smaller degradations of the RMSE occur (from -0.02 ppm at PUI, to -0.25 ppm at CES).

The central plot in Figure 11 shows a comparison of the RMSE reduction at the sites with other inversions, but also the evolution of the model-observation biases for inversion Rref (blue lines, right axis). The posterior biases at OXK and OPE are respectively 3.19 ppm (prior: 2.00) and 2.83 ppm (prior: -0.37). Meanwhile the posterior biases of neighbouring sites HEI and SSL are respectively -1.81 ppm (prior -3.48) and -1.22 ppm (prior -1.67). The observation sites are close to each other and

25
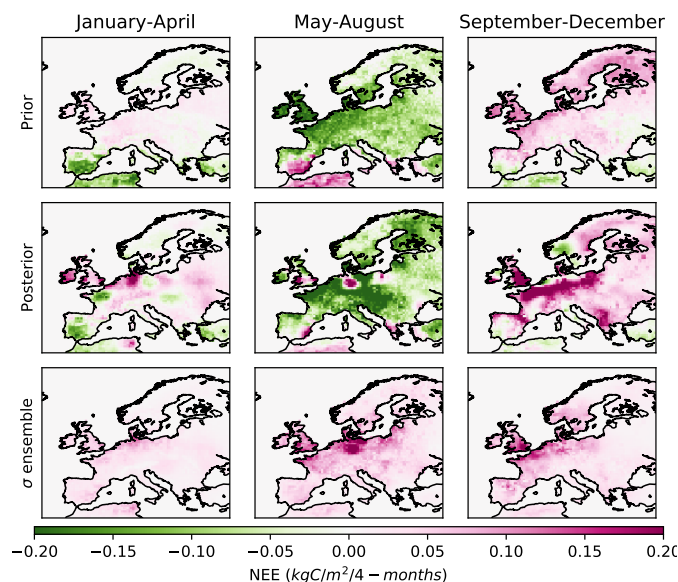
Figure 10. Prior (top) and posterior (middle) NEE in the Rref (reference) scenario, in three four-months periods (JFMA, MJJA, SOND); Variability (standard deviation) of the posterior fluxes across the ensemble of simulations (Rref, R500, R100, RP, RA, Rlf)

sample largely the same air masses; it is not possible for the inversion to find a combination of fluxes that improves the fit at all sites (at least not without departing too much from the prior).

530   Likely causes for these poor misfit reductions are transport model errors (diverging biases at neighbouring sites, introduced either by the foreground transport model (FLEXPART) or by the background one (TM5-4DVAR)) and/or a locally insufficient resolution of the optimized state vector. These causes will need to be investigated thoroughly im a future study, but are not a sign of a malfunction of the optimization method itself.

6   Discussion

We have setup an atmospheric inversion system based on an implementation of the variational inversion approach (Section 535 3.1) with a transport model based on an offline coupling between FLEXPART (high-resolution regional transport) and TM5 (coarse-resolution transport of the background fluxes and historical atmospheric CO_2 burden). The inversion was tested through a series of synthetic experiments and realistic inversions, which show that it is working as expected. In this section we discuss separately three aspects of the paper. First the inversion results themselves, then the TM5-FLEXPART coupling and finally the LUMIA system.
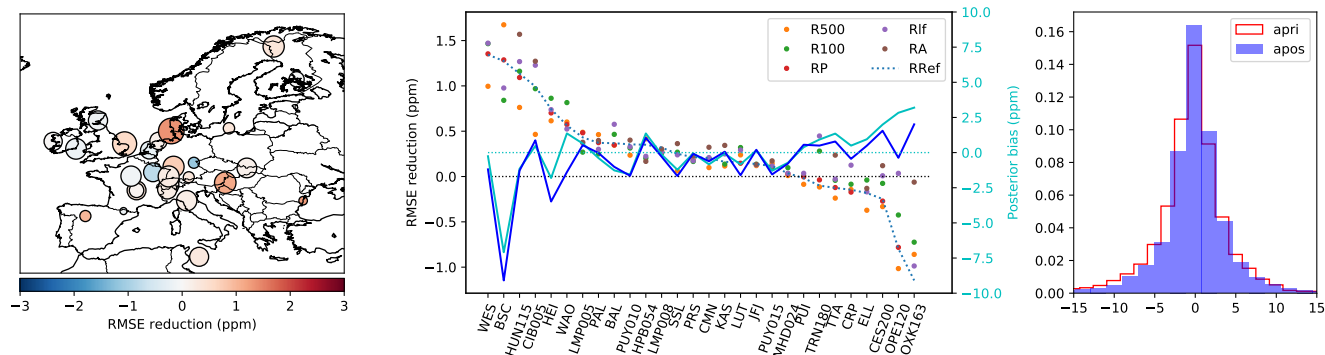
Figure 11. Left: Map of the observation sites in Rref, with the area of the dots proportional to the number of assimilated observation at each site, and the color proportional to the RMSE reduction (prior RMSE minus posterior RMSE). Center: RMSE reduction at each site, for the five sensitivity OSSEs. Right: Prior and posterior distribution of the observation mismatches in Rref (irrespective of the site)
.

6.1 Inversion approach and results

The inversion technique used in this study is by design not innovative (the definition of the control vector, the specification of the uncertainties, etc. replicate what has been done in previous studies (e.g. Kountouris et al. (2018)), as the aim is to have a reference setup. The scientific results are therefore at this stage limited (as it also wasn't the aim of the paper), but the analysis of the OSSEs results show that the inversions are working as expected. Fluxes are well resolved at the monthly scale and large error reductions (with respect to the known truth) occur where the network is the densest, as expected.

The aggregated annual flux estimates are, on the contrary, generally degraded by the inversions compared to the prior. This is because, while both positive and negative prior errors are correctly adjusted in the inversions, the error reduction is much stronger in summer (when the prior strongly overestimates the (prescribed) carbon uptake). The OSSEs are an ideal setup for such studies with no transport and no observational errors, such that this bias in the annual posterior NEE results entirely from uneven seasonal constraints on the flux adjustments (the prior uncertainties are larger in summer than in winter, because NEE is larger in summer).

As mentioned earlier, the focus of the paper is not on the inversion results themselves, and the results shown here might be a worst case scenario: scaling the prior uncertainty to the respiration instead of to the NEE itself, as done here, would for instance partly even out the uncertainties. Nonetheless, the results have potential implications for existing inversions (in the absence of a known truth, it is very difficult to tell how adapted is a particular prior error covariance matrix to a given problem), which makes it a worthy topic for a dedicated study.

The application of the same inversion approach to real observations leads to smaller flux adjustments. This could be a sign that the difference between the LPJ-GUESS prior (used in this second set of inversions) and the true fluxes is smaller than that between the prior and synthetic truth in the OSSEs, but the analysis of the observation misfits reduction also point to potential site-dependent transport model errors. One of the next steps towards improving our inversions will therefore have to be a

thorough model calibration effort. In that sense, the flexibility of LUMIA with regards to the transport model is particularly adapted.

6.2 TM5-FLEXPART coupling

The inversions rely on an offline coupling between the FLEXPART Lagrangian transport model (for regional, high resolution
565 transport) and TM5-4DVAR for providing background concentrations. The setup replicates the 2-step scheme of Rödenbeck et al. (2009) but with different models.

A succint comparison between this "TM5-FLEXPART" transport model and TM5 itself was performed (Section 3.3.1) and is used as a proxy for the transport model error. It doesn't show any global bias between the two models, but a possible seasonal offset towards the month of November. The prescribed observation uncertainties are scaled up to account for this possible
570 larger model error, so the impact on inversions should be limited. Nonetheless, that possible seasonal bias would need to be investigated and accounted for before deriving scientific conclusions from inversions against real observations.

The choice of the models and of that specific coupling was driven in part by the perspective of exchanges with other groups using similar setups. In the current stage, replacing the FLEXPART response functions from another similar Lagrangian transport model (STILT (), NAME (), etc.) or the TM5 background time series by data generated with a different model (using
575 either the same or a different technique to estimate background concentrations at the observation sites) is straightforward and will facilitate a better evaluation of the model performance.

Note also that the Rödenbeck et al. (2009) approach means that there is no 'hard' coupling between the two models meaning that there is no risk of having to use an older version of one model because of the lack of implementation of the coupling in newer code. This, of course, also facilitates the exchange of one transport model against another as mentioned above.
580 From a practical and technical point of view, the current setup presents the advantage of speed and scalability: the application of the transport operator is done independently for each observation and therefore can be distributed on as many CPUs as available. Inversions can thus be performed in very limited (user) time (5-8 hours wall time per inversion on 24 CPUs for the inversions in this paper). This time efficiency is critical for running not only single inversions, but inversion ensembles, which provide a better representation of the real uncertainties. Evolutions of the code for very large ensemble of observations
585 (such as from satellite retrievals) may, however, benefit from further developments (aggregation of observations and footprints; reduction of the number of grid points where possible; etc.)

6.3 LUMIA framework

LUMIA is primarily designed as a library of (python) code to support the development of inverse modelling activities at Lund University. It aims at being not an integrated atmospheric inversion system (i.e. transport model + inversion algorithm), but
590 rather a toolbox for inversions (and for model-data fusion approaches in general). Currently, the available code is mainly limited to the modules used in the inversions presented in this paper, but applications such as inversions with other tracers (CH_4, $^{14}CO_2$), with other regional transport models (STILT) and coupling with a vegetation model (towards a CCDAS) are envisioned.

595   The existing (and future) modules are build with the aim to maximize flexibility (i.e. the capacity for the user to build their own inversion experiments, rather than just replicate existing ones), usability and sustainability of the code. The concept of usability refers to the need to limit the time spent by users in understanding the code itself (rather than the algorithms implemented in the code), while the concept of sustainability refers to the capacity for the code to retain its flexibility and usability characteristics throughout future developments. Concretely, it means that the code should attempt to follow a number of simple but essential coding practices (one function, one task; explicit naming of variables; code as close as possible as

600   the original equations; clean I/O; usage of only standard libraries to facilitate portability, etc.). The aim is in particular that a module can be removed/replaced without risking to break other modules.

The LUMIA code is not meant to be a "key in hand" system, it targets users having or willing to acquire robust understanding of inverse modelling (it is perfectly usable as a toy model for learning). We therefore do not publish the code in a public repository, but we are very open to collaborations and distribute the code on-demand. An archive of the code in it's current

605   shape is nonetheless included as SI of this document.

7   Summary and conclusions

We have presented the LUMIA inversion library, as well as a first set of regional CO_2 inversions performed with LUMIA, relying on a new coupling between the FLEXPART and TM5-4DVAR transport model. LUMIA is designed to be a toolbox for inversions and is meant to support future inverse modelling work at Lund University.

610   The inversions intentionally follow a very classical approach, so as to facilitate comparison with other systems and to set a point of reference. The aim is, however, to use LUMIA in the future to develop more innovative approaches (multiple transport models, use of satellite data, optimisation of vegetation model parameters (CCDAS), etc.).

Although the inversion setup lacks the maturity of established systems, it offers promising computational performances and the results suggest interesting scientific questions regarding the capacity of regional inversion systems to constrain the annual

615   budget of CO_2, and point to specific improvements of the inversion approach.

Author contributions.   G.M. and M.S designed the experiments and G.M. developped the code and performed the simulations. G.M. prepared the manuscript and M.S. provided corrections and suggestions for improvements.

References

BP: Statistical Review of World Energy 2016, Tech. rep., http://www.bp.com/content/dam/bp/excel/energy-economics/statistical-review-2016/bp-statistical-review-of-world-energy-2016-workbook.xls, 2016.

Basu, S., Guerlet, S., Butz, A., Houweling, S., Hasekamp, O., Aben, I., Krummel, P., Steele, P., Langenfelds, R., Torn, M., Biraud, S., Stephens, B., Andrews, A., and Worthy, D.: Global CO_2 fluxes estimated from GOSAT retrievals of total column CO_2, Atmospheric Chemistry and Physics, 13, 8695–8717, https://doi.org/10.5194/acp-13-8695-2013, http://www.atmos-chem-phys.net/13/8695/2013/, 2013a.

Basu, S., Guerlet, S., Butz, A., Houweling, S., Hasekamp, O., Aben, I., Krummel, P., Steele, P., Langenfelds, R., Torn, M., Biraud, S., Stephens, B., Andrews, A., and Worthy, D.: Global CO_2 fluxes estimated from GOSAT retrievals of total column CO_2, Atmospheric Chemistry and Physics, 13, 8695–8717, https://doi.org/10.5194/acp-13-8695-2013, http://www.atmos-chem-phys.net/13/8695/2013/, 2013b.

Chevallier, F., Fisher, M., Peylin, P., Serrar, S., Bousquet, P., Bréon, F.-M., Chédin, A., and Ciais, P.: Inferring CO_2 sources and sinks from satellite observations: Method and application to TOVS data, Journal of Geophysical Research, 110, D24 309, https://doi.org/10.1029/2005JD006390, 2005.

Ciais, P., Crisp, D., Denier van der Gon, H., Engelen, R., Janssens-Maenhout, G., Heimann, M., Rayner, P., and Scholze, M.: Towards a European Operational Observing System to Monitor Fossil CO_2 emissions - Final Report from the expert group, vol. 19, European Commission, Copernicus Climate Change Service, https://www.copernicus.eu/sites/default/files/2018-10/CO2{_}Report{_}22Oct2015.pdf, 2015.

Ciattaglia, L., Cundari, V., and Colombo, T.: Further measurements of atmospheric carbon dioxide at Mt. Cimone, Italy: 1979–1985, Tellus B, 39 B, 13–20, https://doi.org/10.1111/j.1600-0889.1987.tb00266.x, 1987.

Courtier, P., Thépaut, J.-N., and Hollingsworth, A.: A strategy for operational implementation of 4D-Var, using an incremental approach, Q. J. R. Mereorol Soc, 120, 1367–1387, http://onlinelibrary.wiley.com/doi/10.1002/qj.49712051912/abstract, 1994.

Denier van der Gon, H. D., Hendriks, C., Kuenen, J., Segers, A., and Visschedijk, A.: Description of current temporal emission patterns and sensitivity of predicted AQ for temporal emission patterns, in: EU FP7 MACC deliverable report D_D-EMIS_1.3, https://gmes-atmosphere.eu/documents/deliverables/d-emis/MACC{_}TNO{_}del{_}1{_}3{_}v2.pdf, 2016.

Dlugokencky, E., Mund, J. M., Crotwell, A., Crotwell, M., and Thoning, K.: Atmospheric Carbon Dioxide Dry Air Mole Fractions from the NOAA ESRL Carbon Cycle Cooperative Global Air Sampling Network, 1968-2018, Version: 2019-07, https://doi.org/https://doi.org/10.15138/wkgj-f215, 2019.

Errico, R. M.: What Is an Adjoint Model ?, Bulletin of the American Meteorological Society, 78, 2577–2591, 1997.

Farquhar, G. D., von Caemmerer, S., and Berry, J. A.: A biochemical model of photosynthetic CO_2 assimilation in leaves of C3 species, Planta, 149, 78–90, https://doi.org/10.1007/BF00386231, https://doi.org/10.1007/BF00386231, 1980.

Ganesan, A. L., Manning, A. J., Grant, A., Young, D., Oram, D. E., Sturges, W. T., Moncrieff, J. B., and O'Doherty, S.: Quantifying methane and nitrous oxide emissions from the UK and Ireland using a national-scale monitoring network, Atmospheric Chemistry and Physics, 15, 6393–6406, https://doi.org/10.5194/acp-15-6393-2015, http://www.atmos-chem-phys.net/15/6393/2015/, 2015.

Giglio, L., Randerson, J. T., and Van Der Werf, G. R.: Analysis of daily, monthly, and annual burned area using the fourth-generation global fire emissions database (GFED4), Journal of Geophysical Research: Biogeosciences, 118, 317–328, https://doi.org/10.1002/jgrg.20042, 2013.

Gurney, K. R., Law, R. M., Denning, A. S., Rayner, P. J., Baker, D., Bousquet, P., Bruhwiler, L., Chen, Y. H., Ciais, P., Fan, S., Fung, I. Y., Gloor, M., Heimann, M., Higuchi, K., John, J., Maki, T., Maksyutov, S., Masarie, K., Peylin, P., Prather, M., Pak, B. C., Randerson, J.,

Sarmiento, J., Taguchi, S., Takahashi, T., and Yuen, C. W.: Towards robust regional estimates of annual mean {CO}_2 sources and sinks, Nature, 415, 626–630, 2002.

Hammer, S., Glatzel Mattheier, H., Müller, L., Sabasch, M., Schmidt, M., Schmitt, S., Schönherr, C., Vogel, F., Worthy, D., and Levin, I.: A gas chromatographic system for high-precision quasi-continuous atmospheric measurements of CO2, CH4, N2O, SF6, CO and H2., 2008.

Haszpra, L., Barcza, Z., Bakwin, P., Berger, B., Davis, K. J., and Weidinger, T.: Measuring system for the long-term monitoring of biosphere/atmosphere exchange of carbon dioxide, Journal of Geophysical Research Atmospheres, 106, 3057–3069, https://doi.org/10.1029/2000JD900600, 2001.

Hatakka, J., Aalto, T., Aaltonen, V., Aurela, M., Hakola, H., Komppula, M., Laurila, T., Lihavainen, H., Paatero, J., Salminen, K., and Viisanen, Y.: Overview of the atmospheric research activities and results at Pallas GAW station, Boreal Environment Research, 8, 365–383, 2003.

Houweling, S., Krol, M., Bergamaschi, P., Frankenberg, C., Dlugokencky, E. J., Morino, I., Notholt, J., Sherlock, V., Wunch, D., Beck, V., Gerbig, C., Chen, H., Kort, E. A., Röckmann, T., and Aben, I.: A multi-year methane inversion using SCIAMACHY, accounting for systematic errors using TCCON measurements, Atmospheric Chemistry and Physics, 14, 3991–4012, https://doi.org/10.5194/acp-14-3991-2014, https://www.atmos-chem-phys.net/14/3991/2014/, 2014.

Huijnen, V., Williams, J., Van Weele, M., Van Noije, T., Krol, M., Dentener, F., Segers, A., Houweling, S., Peters, W., De Laat, J., Boersma, F., Bergamaschi, P., Van Velthoven, P., Le Sager, P., Eskes, H., Alkemade, F., Scheele, R., Nédélec, P., and Pätz, H. W.: The global chemistry transport model TM5: Description and evaluation of the tropospheric chemistry version 3.0, Geoscientific Model Development, 3, 445–473, https://doi.org/10.5194/gmd-3-445-2010, 2010.

Hurtt, G. C., Chini, L. P., Frolking, S., Betts, R. A., Feddema, J., Fischer, G., Fisk, J. P., Hibbard, K., Houghton, R. A., Janetos, A., Jones, C. D., Kindermann, G., Kinoshita, T., Klein Goldewijk, K., Riahi, K., Shevliakova, E., Smith, S., Stehfest, E., Thomson, A., Thornton, P., van Vuuren, D. P., and Wang, Y. P.: Harmonization of land-use scenarios for the period 1500-2100: 600 years of global gridded annual land-use transitions, wood harvest, and resulting secondary lands, Climatic Change, 109, 117–161, https://doi.org/10.1007/s10584-011-0153-2, 2011.

Janssens-Maenhout, G., Crippa, M., Guizzardi, D., Muntean, M., Schaaf, E., Dentener, F., Bergamaschi, P., Pagliari, V., Olivier, J. G. J., Peters, J. A. H. W., van Aardenne, J. A., Monni, S., Doering, U., Petrescu, A. M. R., Solazzo, E., and Oreggioni, G. D.: EDGAR v4.3.2 Global Atlas of the three major greenhouse gas emissions for the period 1970–2012, Earth System Science Data, 11, 959–1002, https://doi.org/10.5194/essd-11-959-2019, https://www.earth-syst-sci-data.net/11/959/2019/, 2019.

Kaminski, T., Knorr, W., Schürmann, G., Scholze, M., Rayner, P. J., Zaehle, S., Blessing, S., Dorigo, W., Gayler, V., Giering, R., Gobron, N., Grant, J. P., Heimann, M., Hooker-Stroud, A., Houweling, S., Kato, T., Kattge, J., Kelley, D., Kemp, S., Koffi, E. N., Köstler, C., Mathieu, P. P., Pinty, B., Reick, C. H., Rödenbeck, C., Schnur, R., Scipal, K., Sebald, C., Stacke, T., Van Scheltinga, A. T., Vossbeck, M., Widmann, H., and Ziehn, T.: The BETHY/JSBACH Carbon Cycle Data Assimilation System: Experiences and challenges, Journal of Geophysical Research: Biogeosciences, 118, 1414–1426, https://doi.org/10.1002/jgrg.20118, 2013.

Kountouris, P., Gerbig, C., Rödenbeck, C., Karstens, U., Koch, T. F., and Heimann, M.: Technical Note: Atmospheric CO<sub>2</sub> inversions on the mesoscale using data-driven prior uncertainties: methodology and system evaluation, Atmospheric Chemistry and Physics, 18, 3027–3045, https://doi.org/10.5194/acp-18-3027-2018, https://www.atmos-chem-phys.net/18/3027/2018/, 2018.

Krinner, G., Viovy, N., de Noblet-Ducoudré, N., Ogée, J., Polcher, J., Friedlingstein, P., Ciais, P., Sitch, S., and Prentice, I. C.: A dynamic global vegetation model for studies of the coupled atmosphere-biosphere system, Global Biogeochemical Cycles, 19, 1–33,

705   https://doi.org/10.1029/2003GB002199, 2005.

Lanczos, C.: An Iteration Method for the Solution of the Eigenvalue Problem of Linear Differential and Integral Operators, Journal Of Research Of The National Bureau Of Standards, 45, 255–282, 1950.

Le Quéré, C., Andrew, R. M., Friedlingstein, P., Sitch, S., Hauck, J., Pongratz, J., Pickers, P. A., Korsbakken, J. I., Peters, G. P., Canadell, J. G., Arneth, A., Arora, V. K., Barbero, L., Bastos, A., Bopp, L., Chevallier, F., Chini, L. P., Ciais, P., Doney, S. C., Gkritzalis, T., Goll,

710   D. S., Harris, I., Haverd, V., Hoffman, F. M., Hoppema, M., Houghton, R. A., Hurtt, G., Ilyina, T., Jain, A. K., Johannessen, T., Jones, C. D., Kato, E., Keeling, R. F., Goldewijk, K. K., Landschützer, P., Lefèvre, N., Lienert, S., Liu, Z., Lombardozzi, D., Metzl, N., Munro, D. R., Nabel, J. E. M. S., Nakaoka, S.-i., Neill, C., Olsen, A., Ono, T., Patra, P., Peregon, A., Peters, W., Peylin, P., Pfeil, B., Pierrot, D., Poulter, B., Rehder, G., Resplandy, L., Robertson, E., Rocher, M., Rödenbeck, C., Schuster, U., Schwinger, J., Séférian, R., Skjelvan, I., Steinhoff, T., Sutton, A., Tans, P. P., Tian, H., Tilbrook, B., Tubiello, F. N., van der Laan-Luijkx, I. T., van der Werf, G. R., Viovy,

715   N., Walker, A. P., Wiltshire, A. J., Wright, R., Zaehle, S., and Zheng, B.: Global Carbon Budget 2018, Earth System Science Data, 10, 2141–2194, https://doi.org/10.5194/essd-10-2141-2018, https://www.earth-syst-sci-data.net/10/2141/2018/, 2018.

Meirink, J. F., Bergamaschi, P., and Krol, M. C.: Four-dimensional variational data assimilation for inverse modelling of atmospheric methane emissions: method and comparison with synthesis inversion, Atmospheric Chemistry and Physics, 8, 6341–6353, 2008.

Michalak, A. M., Randazzo, N. A., and Chevallier, F.: Diagnostic methods for atmospheric inversions of long-lived greenhouse gases,

720   Atmospheric Chemistry and Physics, 17, 7405–7421, https://doi.org/10.5194/acp-17-7405-2017, https://www.atmos-chem-phys.net/17/7405/2017/, 2017.

NOAA Carbon Cycle Group ObsPack Team: Multi-laboratory compilation of atmospheric methane data for the period 1957-2017; obspack_ch4_1_GLOBALVIEWplus_v1.0_2019_01_08;, https://doi.org/https://doi.org/10.25925/20190108, https://www.esrl.noaa.gov/gmd/ccgg/obspack/data.php?id=obspack{_}ch4{_}1{_}GLOBALVIEWplus{_}v1.0{_}2019-01-08, 2019.

725   Peters, W., Jacobson, A. R., Sweeney, C., Andrews, A. E., Conway, T. J., Masarie, K., Miller, J. B., Bruhwiler, L. M. P., Pétron, G., Hirsch, A. I., Worthy, D. E. J., van der Werf, G. R., Randerson, J. T., Wennberg, P. O., Krol, M. C., and Tans, P. P.: An atmospheric perspective on North American carbon dioxide exchange: CarbonTracker., Proceedings of the National Academy of Sciences of the United States of America, 104, 18 925–18 930, https://doi.org/10.1073/pnas.0708986104, http://www.pubmedcentral.nih.gov/articlerender.fcgi?artid=2141884{&}tool=pmcentrez{&}rendertype=abstract, 2007.

730   Peylin, P., Law, R. M., Gurney, K. R., Chevallier, F., Jacobson, A. R., Maki, T., Niwa, Y., Patra, P. K., Peters, W., Rayner, P. J., Rödenbeck, C., Van Der Laan-Luijkx, I. T., and Zhang, X.: Global atmospheric carbon budget: Results from an ensemble of atmospheric CO2 inversions, Biogeosciences, 10, 6699–6720, https://doi.org/10.5194/bg-10-6699-2013, 2013.

Pisso, I., Sollum, E., Grythe, H., Kristiansen, N., Cassiani, M., Eckhardt, S., Arnold, D., Morton, D., Thompson, R. L., Groot Zwaaftink, C. D., Evangeliou, N., Sodemann, H., Haimberger, L., Henne, S., Brunner, D., Burkhart, J. F., Fouilloux, A., Brioude, J., Philipp, A., Seib-

735   ert, P., and Stohl, A.: The Lagrangian particle dispersion model FLEXPART version 10.3, Geoscientific Model Development Discussions, pp. 1–67, https://doi.org/10.5194/gmd-2018-333, https://www.geosci-model-dev-discuss.net/gmd-2018-333/, 2019.

Rayner, P. J., Michalak, A. M., and Chevallier, F.: Fundamentals of Data Assimilation applied to biogeochemistry, Atmospheric Chemistry and Physics Discussions, pp. 1–32, https://doi.org/10.5194/acp-2018-1081, https://www.atmos-chem-phys-discuss.net/acp-2018-1081/, 2018.

740 Rödenbeck, C., Gerbig, C., Trusilova, K., and Heimann, M.: A two-step scheme for high-resolution regional atmospheric trace gas inversions based on independent models, Atmospheric Chemistry and Physics Discussions, 9, 1727–1756, https://doi.org/10.5194/acpd-9-1727-2009, 2009.

Rödenbeck, C., Keeling, R. F., Bakker, D. C., Metzl, N., Olsen, A., Sabine, C., and Heimann, M.: Global surface-ocean pCO2 and sea-Air CO2 flux variability from an observation-driven ocean mixed-layer scheme, Ocean Science, 9, 193–216, https://doi.org/10.5194/os-9-193-

745 2013, 2013.

Rozanski, K., Necki, J., Chmura, L., Sliwka, I., Zimnoch, M., Bielewski, J., Galkowski, M., Bartyzel, J., and Rosiek, J.: Anthropogenic changes of CO2, CH4, N2O, CFCl3, CF2Cl2, CCl2FCClF2, CHCl3, CH3CCl3, CCl4, SF6 and SF5CF3 mixing ratios in the atmosphere over southern Poland, Geological Quarterly, 58, https://doi.org/10.7306/gq.1163, 2014.

Schaefer, K., Collatz, G. J., Tans, P., Denning, A. S., Baker, I., Berry, J., Prihodko, L., Suits, N., and Philpott, A.: Combined simple

750 biosphere/carnegie-ames-stanford approach terrestrial carbon cycle model, Journal of Geophysical Research: Biogeosciences, 113, 1–13, https://doi.org/10.1029/2007JG000603, 2008.

Schmidt, M.: The Schauinsland CO$_2$ record: 30 years of continental observations and their implications for the variability of the European CO$_2$ budget, Journal of Geophysical Research, 108, 1–7, https://doi.org/10.1029/2002jd003085, 2003.

Seibert, P. and Frank, a.: Source-receptor matrix calculation with a Lagrangian particle dispersion model in backward mode, Atmospheric

755 Chemistry and Physics, 4, 51–63, https://doi.org/10.5194/acp-4-51-2004, 2004.

Sitch, S., Friedlingstein, P., Gruber, N., Jones, S. D., Murray-Tortarolo, G., Ahlström, A., Doney, S. C., Graven, H., Heinze, C., Huntingford, C., Levis, S., Levy, P. E., Lomas, M., Poulter, B., Viovy, N., Zaehle, S., Zeng, N., Arneth, A., Bonan, G., Bopp, L., Canadell, J. G., Chevallier, F., Ciais, P., Ellis, R., Gloor, M., Peylin, P., Piao, S. L., Le Quéré, C., Smith, B., Zhu, Z., and Myneni, R.: Recent trends and drivers of regional sources and sinks of carbon dioxide, Biogeosciences, 12, 653–679, https://doi.org/10.5194/bg-12-653-2015, https:

760 //www.biogeosciences.net/12/653/2015/, 2015.

Smith, B., Wärlind, D., Arneth, A., Hickler, T., Leadley, P., Siltberg, J., and Zaehle, S.: Implications of incorporating N cycling and N limitations on primary production in an individual-based dynamic vegetation model, Biogeosciences, 11, 2027–2054, https://doi.org/10.5194/bg-11-2027-2014, 2014.

Steinbach, J., Gerbig, C., Rödenbeck, C., Karstens, U., Minejima, C., and Mukai, H.: The CO2 release and Oxygen uptake from Fossil

765 Fuel Emission Estimate (COFFEE) dataset: effects from varying oxidative ratios, Atmospheric Chemistry and Physics, 11, 6855–6870, https://doi.org/10.5194/acp-11-6855-2011, https://www.atmos-chem-phys.net/11/6855/2011/, 2011.

Stocker, T. F., Qin, D., Plattner, G.-K., Tignor, M., Allen, S., Boschung, J., Nauels, A., Xia, Y., Bex, V., and Midgley, P.: Climate Change 2013: The Physical Science Basis. Contribution of Working Group I to the Fifth Assessment Report of the Intergovernmental Panel on Climate Change, in: IPCC, 2013, Cambridge University Press, Cambridge, United Kingdom and New York, NY, USA, 2013.

770 Stohl, A., Sodemann, H., Eckhardt, S., Frank, A., Seibert, P., and Wotawa, G.: The Lagrangian particle dispersion model FLEXPART version 8.2, Tech. rep., 2010.

Takahashi, T., Sutherland, S. C., Wanninkhof, R., Sweeney, C., Feely, R. A., Chipman, D. W., Hales, B., Friederich, G., Chavez, F., Sabine, C., Watson, A., Bakker, D. C., Schuster, U., Yoshikawa-Inoue, H., Ishii, M., Midorikawa, T., Nojiri, Y., Körtzinger, A., Steinhoff, T., Hoppema, M., Olafsson, J., Arnarson, T. S., Johannessen, T., Olsen, A., Bellerby, R., Wong, C., Delille, B., Bates, N., and de Baar, H. J.:

775 Climatological mean and decadal change in surface ocean pCO2, and net sea–air CO2 flux over the global oceans, Deep Sea Research Part II: Topical Studies in Oceanography, 56, 554–577, https://doi.org/10.1016/J.DSR2.2008.12.009, https://www.sciencedirect.com/science/article/pii/S0967064508004311, 2009.

Thompson, R. L., Stohl, A., Zhou, L. X., Dlugokencky, E., Fukuyama, Y., Tohjima, Y., Kim, S. Y., Lee, H., Nisbet, E. G., Fisher, R. E., Lowry, D., Weiss, R. F., Prinn, R. G., O'Doherty, S., Young, D., and White, J. W.: Methane emissions in East Asia for 2000-2011 estimated using

780   an atmospheric Bayesian inversion, Journal of Geophysical Research, 120, 4352–4369, https://doi.org/10.1002/2014JD022394, 2015.

Uglietti, C., Leuenberger, M., and Brunner, D.: European source and sink areas of CO2 retrieved from Lagrangian transport model interpretation of combined O2 and CO2 measurements at the high alpine research station Jungfraujoch, Atmospheric Chemistry and Physics, 11, 8017–8036, https://doi.org/10.5194/acp-11-8017-2011, 2011.

van der Laan, S., Neubert, R. E. M., and Meijer, H. A. J.: A single gas chromatograph for accurate atmospheric mixing ratio measurements of

785   CO_2, CH_4, N_2O, SF_6 and CO, Atmospheric Measurement Techniques Discussions, 2, 1321–1349, https://doi.org/10.5194/amtd-2-1321-2009, 2009.

Van Der Werf, G. R., Randerson, J. T., Giglio, L., Van Leeuwen, T. T., Chen, Y., Rogers, B. M., Mu, M., Van Marle, M. J., Morton, D. C., Collatz, G. J., Yokelson, R. J., and Kasibhatla, P. S.: Global fire emissions estimates during 1997-2016, Earth System Science Data, 9, 697–720, https://doi.org/10.5194/essd-9-697-2017, 2017.

790   Vermeulen, a. T., Hensen, a., Popa, M. E., Van Den Bulk, W. C. M., and Jongejan, P. a. C.: Greenhouse gas observations from Cabauw Tall Tower (1992-2010), Atmospheric Measurement Techniques, 4, 617–644, https://doi.org/10.5194/amt-4-617-2011, 2011.

Weedon, G. P., Balsamo, G., Bellouin, N., Gomes, S., Best, M. J., and Viterbo, P.: Data methodology applied to ERA-Interim reanalysis data, Water Resources Research, 50, 7505–7514, https://doi.org/10.1002/2014WR015638.Received, 2014.

Wilson, P.: Insight into the Carbon Cycle from Continuous Measurements of Oxygen and Carbon Dioxide at Weybourne Atmospheric

795   Observatory , UK, Ph.D. thesis, University of East Anglia, 2012.

Yver, C., Schmidt, M., Bousquet, P., and Ramonet, M.: Measurements of molecular hydrogen and carbon monoxide on the Trainou tall tower, Tellus, Series B: Chemical and Physical Meteorology, 63, 52–63, https://doi.org/10.1111/j.1600-0889.2010.00520.x, 2011.